Total Ozone Mapping by Integrating Databases From Remote Sensing Instruments and Empirical Models

George Christakos, Alexander Kolovos, Marc L. Serre, and Fred Vukovich

***Abstract*—Atmospheric studies often require the generation of high-resolution maps of ozone distribution across space and time. The high natural variability of ozone concentrations and the different levels of accuracy of the algorithms used to generate data from remote sensing instruments introduce major sources of uncertainty in ozone modeling and mapping. These aspects of atmospheric ozone distribution cannot be confronted satisfactorily by means of conventional interpolation and statistical data analysis. We suggest that the techniques of Modern Spatiotemporal Geostatistics (MSG) can be used efficiently to integrate salient (although of varying uncertainty) physical knowledge bases about atmospheric ozone in order to generate and update realistic pictures of ozone distribution across space and time. The MSG techniques rely on a powerful scientific methodology that does not make the restrictive modeling assumptions of previous techniques. A numerical study is discussed involving datasets generated by measuring instruments onboard the Nimbus 7 satellite. In addition to exact (hard) ozone data, the MSG techniques process uncertain measurements and secondary (soft) information in terms of total ozone-tropopause pressure empirical relationships. Nonlinear estimators are used, in general, and non-Gaussian probability laws are automatically incorporated. The proposed total ozone analysis can take into consideration major sources of error in the Total Ozone Mapping Spectrometer solar backscatter ultraviolet tropospheric ozone residual (related to data sampling, etc.) and produce high spatial resolution maps that are more accurate and informative than those obtained by conventional interpolation techniques.**

***Index Terms*—Atmosphere, Bayesian maximum entropy (BME), interpolation, modern geostatistics, ozone, prediction, solar backscatter ultraviolet (SBUV), spatiotemporal, Total Ozone Mapping Spectrometer (TOMS).**

I. Introduction

SINCE THE LATE 1970s, total ozone (TO_3) analyses have been produced on a global basis using data from the Total Ozone Mapping Spectrometer (TOMS). In the last decade, climatological analyses of the tropospheric ozone residual (TOR), which is an estimate of the total tropospheric ozone and which was, in the initial work, the difference between the TO_3 from TOMS and the stratospheric ozone determined from the Stratospheric Aerosol and Gas Experiment (SAGE) instrument, have been developed [18]. TOMS total ozone data are collected globally on a daily basis and are achieved with a spatial resolution of 1° latitude and 1.25° longitude. On the other hand, the integration of years of SAGE data were required to provide a reliable analysis of the stratospheric ozone on a global basis because SAGE provided a very limited number of observations (about 30) on any given day [36]. Subsequently, attempts have been made to develop daily maps of the TOR using data from the solar backscatter ultraviolet (SBUV) remote sensing system, which were used to establish values for the stratospheric ozone on a daily basis. Initially, direct comparison of variations of daily values of the TOMS/SBUVTOR with the variation of the daily values of the surface ozone concentration provided poor correlations [36], [37], even though reasonably good correlations were noted between longer term (monthly, seasonally, and annual), average TOMS/SBUVTOR values, and surface ozone concentrations, as well as between climatological TOMS/SBUVTOR and ozonesonde data [15], [18], [30], [36], [37].

Many of the problems with the TOMS/SBUVTOR had to do with the poor vertical resolution of the SBUV profile information and poor horizontal resolution in the SBUV stratospheric ozone distribution compared to the spatial resolution of the TOMS total ozone distribution. The SBUV instrument provides ozone profiles by measuring ozone in 12 Umkehr layers [2], [21], [36]. Ziemke and Chandra [39] noted that the determination of SBUV ozone profiles depends on the shape of the weighting function, which provides somewhat unreliable information below the stratospheric ozone peak values (i.e., below the 20–25-km level). Fishman and Balok [19] developed an empirical correction technique that improved the distribution of the amount of ozone in the lower stratosphere and troposphere using SBUV data, and in so doing, improved the calculation of the TOMS/SBUVTOR. Their technique modified the SBUV observations in the lowest three Umkehr layers (i.e., the 63.3–127.0-mb layer, the 127.0–253.0-mb layer, and the 253.0–1013-mb layer) by making the SBUV climatology in those layers consistent with ozonesonde data from a particular site (Wallops Island, VA) that they assumed was climatologically representative of the distribution of ozone for their study region, the Eastern United States.

However, one of the major problems in applying SBUV data with TOMS data to develop estimates of the TOR is the differences in spatial resolution. The SBUV instrument is a nonscanning, downward-looking radiometer. Data are only collected with 200-km spatial resolution along the orbital track of the satellite on which the instrument resides. For illustration, the locations of TOMS total ozone measurements obtained on July 6,

Manuscript received November 18, 2002; revised November 5, 2003. This work was supported in part by the National Aeronautics and Space Administration under Grant 60-00RFQ041, in part by the National Institute of Environmental Health Sciences under Grants P42 ES05948 and P30-ES10126, and in part by the Army Research Office under Grant DAAG55-98-1-0289.

G. Christakos, A. Kolovos, and M. L. Serre are with the Center for the Integrated Study of the Environment (CISE), Department of Environmental Science and Engineering, University of North Carolina, Chapel Hill, NC 27599 USA (e-mail: george_christakos@unc.edu).

F. Vukovich is with the Science Applications International Corporation (SAIC), Raleigh, NC 27605 USA.

Digital Object Identifier 10.1109/TGRS.2003.822751

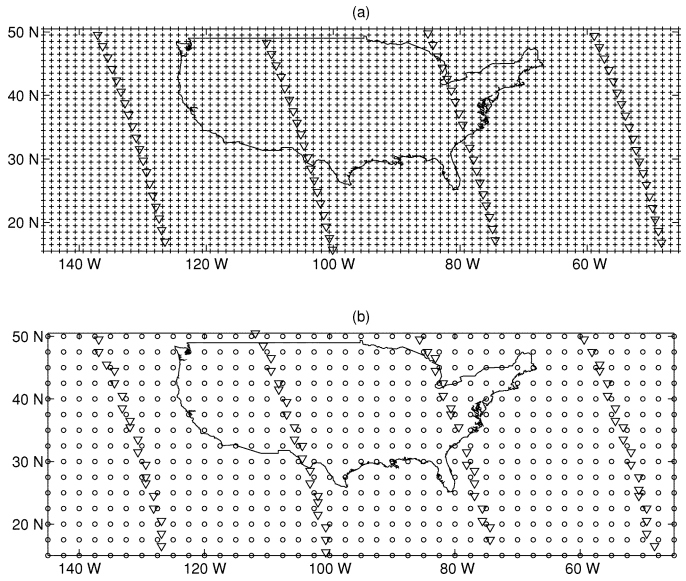

Fig. 1. (a) Grid coverage of satellite ozone measurements for the TOMS (plus markers) and SBUV (triangles) instruments for July 6, 1988. Interpolations are obtained at the TOMS grid points. (b) Locations where hard ozone data were generated for July 6, 1988 using TOMS measurements (triangles) and locations where soft probability ozone data were generated using empirical laws (circles).

1988 are shown in Fig. 1(a) (plus markers). Triangles in Fig. 1(a) indicate the locations of the SBUV measurements on the same day. Clearly, TOMS provides more complete coverage because of its ability to scan while the satellite moves along the orbital track, whereas large SBUV data gaps exist between orbital tracks. The SBUV data gaps have been traditionally filled using conventional interpolation procedures [20] so that stratospheric ozone from the SBUV instrument would be available at the data locations of the TOMS instrument. Fig. 2(a) shows a comparison of stratospheric ozone from the SBUV instrument with the stratospheric ozone derived as the difference between the TOMS total ozone and the tropospheric ozone from the Wallops Island ozonesonde data. The comparison is made only on days when actual SBUV and TOMS measured values, not interpolated data points, were located at the Wallops Island site in the period 1985–1989, so that the stratospheric ozone values were based entirely on measured data. As indicated in the figure, the stratospheric ozone values from the SBUV instrument are highly correlated with the stratospheric ozone derived as the difference between the TOMS total ozone and the tropospheric ozone from ozonesonde data. Fig. 2(b), on the other hand, provides a comparison between stratospheric ozone from the SBUV instrument with the stratospheric ozone derived as the difference between the TOMS total ozone and the tropospheric ozone from the Wallops Island ozonesonde data when only interpolated SBUV data were used to calculate the stratospheric ozone. The poor correlation between the two datasets demonstrates the problem with using conventional interpolation techniques to fill the data gaps between orbital tracks for the SBUV data and also points to a major source of error in the TOMS/SBUVTOR.

As indicated above, the stratospheric ozone variability across space and time, together with the different levels of accuracy attributed to the instruments, introduces considerable sources of uncertainty in the representation of stratospheric ozone distribution when conventional interpolation procedures are used to fill SBUV data gaps. Many of the existing interpolation pro-

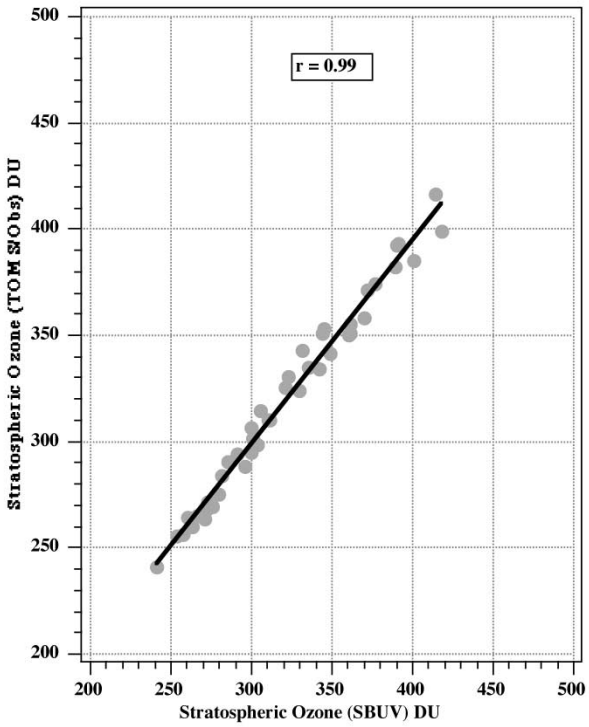

(a)

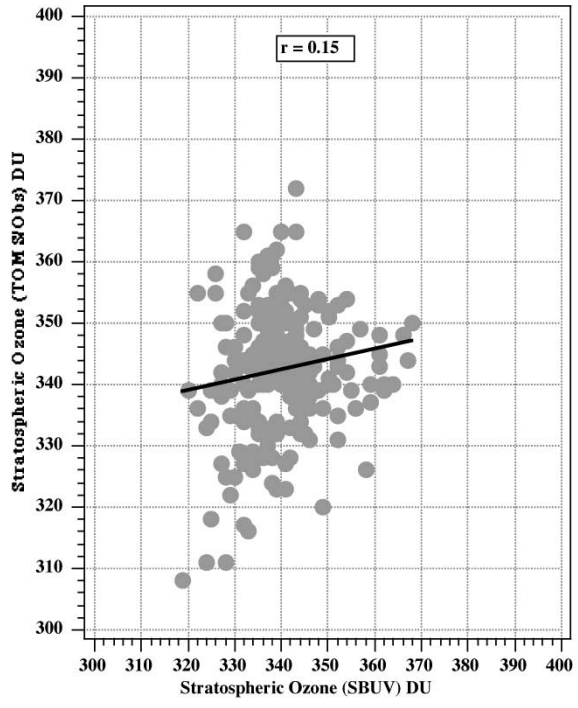

(b)

Fig. 2. (a) Comparison of stratospheric ozone values derived from two different sources at the Wallops Island location for the period 1985–1989. On the vertical axis, TO_3 data come from TOMS and troposphere input from the Wallops Island ozonesonde. On the horizontal axis, the stratospheric ozone values come from the SBUV using matched TOMS and SBUV data. (b) Comparison between derived and interpolated stratospheric ozone values at the Wallops Island location (1985–1989). On the vertical axis, TO_3 data from TOMS and troposphere TO_3 from the Wallops Island ozonesonde have been used. On the horizontal axis, stratospheric ozone from interpolated SBUV data are taken.

cedures that have been used to fill the data gaps (e.g., linear and higher order spatial regression, kriging, basis functions, and neural networks [5], [34]) have lacked the scientific methodology to include rigorously essential sources of physical knowledge and the conceptual organization to account for composite space–time variability effects. Subsequently, these procedures lack the ability to account for features that may exist between SBUV data sampling tracks [3]. The underlying modeling assumptions are too restrictive (e.g., linearity, normality, overparameterization, and physical model independence) and often lead to unrealistic representations of the actual space–time variability of the stratospheric ozone. The information in Fig. 2 indicates the necessity for application of advanced interpolation techniques that provide the theoretical support and technical capabilities to adequately represent the stratospheric ozone variability across space–time and would allow the integration of various knowledge bases that are available about ozone (e.g., data collected at sparse SBUV measurement points, uncertain evidence, and secondary physical information). Such a procedure must be able to interpolate the stratospheric ozone concentrations at unsampled locations with increased accuracy so that the variability across space–time is well represented.

A group of advanced interpolation techniques possessing the desirable features above is provided by modern spatiotemporal geostatistics (MSG): [10]). This paper presents the results from a study on the application of the Bayesian maximum entropy (BME) techniques of MSG to interpolate the ozone at unsampled locations across space to fill SBUV data gaps. BME analysis is based on a sophisticated mathematical theory of space–time interpolation, which does not make any of the restrictive assumptions of conventional interpolation techniques mentioned above. BME gives high priority to a knowledge synthesis system that combines principles of rational reasoning with empirical evidence to improve ozone representation across space and time. This study examined the feasibility of using BME interpolation procedures to obtain better space–time analyses of the SBUV stratospheric ozone. However, no SBUV stratospheric ozone data were used. Instead, the TO_3 obtained nearest to the SBUV measurement locations were analyzed over the continental United States using the BME method. In particular, TOMS' total ozone data at the locations closest to the SBUV sampling points were selected as input for the BME interpolation at unsampled locations. TOMS total ozone was chosen (in particular, TOMS version 7 data) instead of SBUV stratospheric ozone for three reasons. First, the differences in the level of accuracy between the SBUV and TOMS instruments need not be accounted for within the current analysis scope and procedure. Second, data to test the accuracy of the interpolated TO_3 were readily available for the entire domain using all available TOMS data. Data to test the accuracy of the interpolated SBUV stratospheric ozone were not available at the unsampled points, making an evaluation of the interpolated stratospheric ozone field unattainable. Finally, stratospheric ozone makes up at least 85% of the TO_3 and controls its major variations, particularly in the midlatitudes where this study is focused. Presumably, if the procedure improves the analysis of TO_3 obtained at the SBUV measurement locations, then it should also improve the analysis of stratospheric ozone.

Additional secondary information was available for this study. An empirical relationship that relates TO_3 with tropopause pressure was used to take advantage of available model-generated tropopause data from upper air observations. This relationship led to the generation of soft data in the form of probabilistic distributions. The soft data were processed and included in the nonlinear/non-Gaussian BME interpolation scheme at the unsampled locations, and the resulting improvement in TO_3 analysis was investigated. The present paper carries out a series of numerical experiments. First, it focuses on the TO_3 distribution over the continental United States on July 6, 1988. This date was chosen because a major ozone event occurred in the surface layer over the eastern half of the United States in the period July 2–11, 1988, and the ozone characteristics of that event have been studied in great detail both at the surface and aloft. On July 6, 1988, the event was at its peak. The composite space–time BME analysis of TO_3 was compared to the TOMS total ozone analysis for the entire domain and to the TO_3 predictions derived using conventional interpolation techniques. Then, valuable insight about the BME approach was gained by studying its ability to provide a dynamic representation of the TO_3 space–time distributions during successive days (July 7–10, 1988). Finally, BME's prediction power was tested during different months of the year, which allowed us to get a feeling for the large-picture seasonal dependence in the accuracy of the BME analysis.

II. BME Model Description

A. Modern Spatiotemporal Geostatistics

MSG provides a powerful framework for generation of informative, high-resolution maps of atmospheric variables in a composite space–time domain [10], [12]. A thorough review of the MSG theory and techniques is clearly beyond the intended scope of this paper, but a brief exposition of the main concepts is appropriate. Let the vector $\boldsymbol{p} = (\boldsymbol{s}, t)$ define a point in the space–time domain ($\boldsymbol{s}$ is a spatial position vector in the atmosphere and t denotes time). The spatiotemporal random field $X(\boldsymbol{p})$ offers a mathematically rigorous and physically meaningful representation of the ozone distribution across space and time [9]. Ozone studies are generally concerned with the prediction (usually, interpolation) of the TO_3 distribution at a network of points $\boldsymbol{p}_k$, given core knowledge about the entire TO_3 field and a set of site-specific data $\boldsymbol{\chi}_{\text{data}} = (\chi_1, \ldots, \chi_m)$ at points $\boldsymbol{p}_{\text{data}} = (\boldsymbol{p}_1, \ldots, \boldsymbol{p}_m)$. For example, a long-term consistent record of ozone distribution across space is essential to understanding and predicting ozone depletion. At the points $\boldsymbol{p}_k$, either we have no observations at all, or the available data are considerably uncertain and cannot be used as reliable predictions of the actual TO_3 values at these points. In a stochastic interpolation context, one seeks to derive the probability density functions (pdfs) $f_{\text{KB}}(\boldsymbol{\chi}_k)$ that characterize $X(\boldsymbol{p})$ at every node of the mapping grid in light of the physical knowledge sources considered [6], [8]; the subscript KB denotes the knowledge base available (see below also). The TO_3 predictions $\hat{\boldsymbol{\chi}}_k$ at any set of grid nodes $\boldsymbol{p}_k$ are derived from the pdf at the same nodes by means of a suitable criterion. The choice of the criterion is not unique, but it depends on the goals of the study.

In some situations, for example, the criterion may seek the most probable TO_3 predictions; in some other cases, TO_3 predictions may be sought which optimize some cost function, etc. Whatever the criterion selected, the final outcome is a spatiotemporal map that provides a detailed representation of TO_3 distribution in space–time. The unifying epistemic background of the relevant MSG techniques consists of two fundamental tenets.

(Ta) Consider general knowledge bases (herein denoted by $\mathcal{G}$-KB) such as physical laws, governing relationships, primitive equations, and space–time statistical moments (including multiple-point, nonlinear and high-order statistics) to rather abstractly define plausible events and their respective probabilities by means of a *teleologic* (purpose-oriented) principle.

(Tb) Eliminate from consideration those otherwise plausible events that are physically or logically inconsistent with the available site-specific KB (which is denoted as $\mathcal{S}$-KB and may include hard data, uncertain observations, empirical correlations, categorical variables, and fuzzy information). Then, reassign probabilities to the remaining plausible events to be consistent with the $\mathcal{S}$-KB by means of a stochastic logic integration system.

There are two key issues in the MSG conceptual framework above, which are worth discussing. The first issue is the use of a teleologic principle in tenet (Ta). More specifically, the $\mathcal{G}$-KB is properly transformed into a set of integral equations of the corresponding pdf. These integral equations, which are called the teleologic $\mathcal{G}$-equations, are then solved with respect to the pdf. A solution is sought in terms of a purpose or final cause expressed by the action principle. In other words, the form of this solution will depend on the action principle one adopts regarding the events deemed plausible before the available data is considered. Well-known action principles include Aristotle's principle of minimum potential energy, Fermat's principle of least time, and Hamilton's principle of stationary principal function [27]. MSG employs a different kind of an action principle that may be called the principle of *maximum expected information* (note that in previous principles the action sought refers to concepts like energy and time, whereas in the MSG case the action refers to the information concept). The MSG action principle may involve, in particular, the Shannon information measure. Another solution includes the Fisher information measure. Other possibilities exist, as well. In (Tb), the $\mathcal{G}$-based pdf solutions are revised through application of a stochastic logic integration system to yield updated pdf models that are consistent with the available $\mathcal{S}$-KB. Thus, the second key issue is the use of an integration principle to update the probability model derived in tenet (Ta) on the $\mathcal{S}$-KB. In this respect, the MSG framework is very general allowing the use of different inference systems, including statistical inductive inference (e.g., using Bayesian conditionalization) and stochastic deductive inference (e.g., involving material biconditionalization). The choice of a system over another should depend on the physical application considered. In a sense, a central point of the methodological (teleologic and integration) principles above is to provide guidance in order to achieve the cognitive, epistemic, and practical goals of the environmental study.

TABLE I
EXAMPLES OF A $\mathcal{G}$-KB

G-KB	g_α	$\overline{g_\alpha}$
Space-time mean functions	χ_i	$\overline{x_i}$
Space-time covariance functions	$(\chi_i - \overline{x_i})(\chi_j - \overline{x_j})$	$c_x(\boldsymbol{p}_i, \boldsymbol{p}_j)$
Advection-reaction law	$\chi_i(\frac{\partial}{\partial t_i} + v\frac{\partial}{\partial s_i} + \kappa)$	0
	$\chi_i^2(\frac{\partial}{\partial t_i} + v\frac{\partial}{\partial s_i} + 2\kappa)$	0
	$\chi_i\chi_j(\frac{\partial}{\partial t_i} + v\frac{\partial}{\partial s_i} + \kappa)$	0

B. Main BME Steps

As a result of the flexibility regarding the choice of the information concept in (Ta) and the conditionalization principle in (Tb), MSG provides a long list of spatiotemporal analysis and interpolation techniques [13]. The study of TO_3 considered in this paper will focus on the Bayesian maximum-entropy technique of MSG (the terminology will become clear in the sequel), which is perhaps the most widely used at present. In particular, the basic steps of the BME technique are as follows.

Step 1) The general knowledge is expressed in terms of mathematical equations—also known as the teleologic equations—which involve the $\mathcal{G}$–operator and the corresponding pdf $f_{\mathcal{G}}$ (KB $= \mathcal{G}$, in this case) so that

$$\int d\boldsymbol{\chi}_{\text{map}} \mathcal{G}(g_\alpha) f_{\mathcal{G}}(\boldsymbol{\chi}_{\text{map}}) = 0 \quad (\alpha = 1, \ldots, N) \tag{1}$$

where the g_a are properly chosen to express the core physical knowledge considered in the TO_3 study. Various examples of the $\mathcal{G}$-operator of (1) can be found in the relevant MSG literature. In applications in which theoretical and/or empirical equations in terms of statistical moments are available across space–time, the $\mathcal{G}$-operator is given by $\mathcal{G}(g_\alpha) = g_\alpha(\boldsymbol{\chi}_{\text{map}}) - \overline{g_\alpha}(\boldsymbol{p}_{\text{map}})$, where the bar denotes stochastic expectation, $\boldsymbol{p}_{\text{map}} = (\boldsymbol{p}_{\text{data}}, \boldsymbol{p}_k)$, and $\boldsymbol{\chi}_{\text{map}} = (\boldsymbol{\chi}_{\text{data}}, \boldsymbol{\chi}_k)$. In this case, (1) becomes

$$\int d\boldsymbol{\chi}_{\text{map}} [g_\alpha(\boldsymbol{\chi}_{\text{map}}) - \overline{g_\alpha}(\boldsymbol{p}_{\text{map}})] f_{\mathcal{G}}(\boldsymbol{\chi}_{\text{map}}) = 0 \ (\alpha = 1, \ldots, N). \tag{2}$$

By convention, $g_0 = \overline{g}_0 = 1$ (normalization constraint), and the total number N of equations is such that moments are included that involve all the grid points $\boldsymbol{p}_i \in \boldsymbol{p}_{\text{map}}$ of the map (e.g., in the special case that the $\mathcal{G}$-KB provides us with the mean function $\overline{x}_i$ and the covariance function $c_x(\boldsymbol{p}_i, \boldsymbol{p}_j)$ throughout the space–time domain of interest, the selected g_a-functions are shown in Table I). Also in Table I, an example of g_a-functions is given in the

TABLE II
EXAMPLES OF SOFT DATA χ_{soft}

$\boldsymbol{\chi}_{\text{soft}} \in \boldsymbol{I} = (I_{m_h+1},\ldots,I_m)$	(5)
$Prob[\boldsymbol{x}_{\text{soft}} \le \boldsymbol{\zeta}] = F_{\mathcal{S}}(\boldsymbol{\zeta})$	(6)
$Prob[\boldsymbol{x}_{\text{soft}} \le \boldsymbol{\zeta}, \boldsymbol{x}_k \le \boldsymbol{\zeta}_k] = F_{\mathcal{S}}(\boldsymbol{\zeta},\boldsymbol{\zeta}_k)$	(7)

case of the advection–reaction law (X denotes pollutant concentration, v is the fluid velocity, and κ is the reaction rate constant).

Step 2) BME's action principle of choice is expected information maximization in light of the $\mathcal{G}$-KB. The relevant information measure assumed is that of Shannon, in which case the solution of (1) has the generalized maximum entropy form across space–time

$$f_{\mathcal{G}}(\boldsymbol{\chi}_{\text{map}}) = e^{\mu_0 + \boldsymbol{\mu}^T \boldsymbol{g}} \tag{3}$$

where $\boldsymbol{g} = \{g_a; \alpha = 1,\ldots,N\}$ is the vector of g_a-functions above, and $\boldsymbol{\mu} = \{\mu_a; \alpha = 1,\ldots,N\}$ is the vector of coefficients associated with $\boldsymbol{g}$. The μ_a are functions of the space–time coordinates and will be determined in the following step, whereas μ_0 is a coefficient that accounts for the normalization constraint, $\overline{g}_0 = 1$ of the previous step.

Step 3) Substitute (3) into (2) and solve for coefficients $\boldsymbol{\mu}$. Insert these coefficients back into (3) to find the exact form of the $\mathcal{G}$-based pdf model $f_{\mathcal{G}}$ of the TO_3 map.

Step 4) The $\mathcal{S}$-KB may consist of hard TO_3 data at a set of points $\boldsymbol{p}_i (i = 1,\ldots,m_h)$, and soft (uncertain or secondary) data at another set of points $\boldsymbol{p}_i (i = m_h+1,\ldots,m)$, i.e.,

$$\mathcal{S}: \begin{cases} \boldsymbol{\chi}_{\text{hard}} = (\chi_1,\ldots,\chi_{m_h}) \\ \boldsymbol{\chi}_{\text{soft}} = (\chi_{m_h+1},\ldots,\chi_m) \end{cases} \tag{4}$$

such that $\boldsymbol{\chi}_{\text{data}} = (\boldsymbol{\chi}_{\text{hard}}, \boldsymbol{\chi}_{\text{soft}})$. In Table II, for example, the soft data $\boldsymbol{\chi}_{\text{data}}$ may be expressed in terms of intervals of varying lengths [see (5)] and probabilistic functions of arbitrary shapes [see (6)]. Equation (7) corresponds to the case that probabilistic TO_3 data are also available at the interpolation points $\boldsymbol{p}_k$ themselves. Several other types of $\mathcal{S}$-KB are considered in the MSG literature (e.g., [4], [25], and [33]. The hard and soft data ($\mathcal{S}$-KB) are subsequently expressed in terms of the Ξ_S-operator and its domain D. The form of Ξ_S and the shape of D depend on the types of $\mathcal{S}$-KB considered. Some examples are given in Table III.

TABLE III
EXAMPLES OF $\Xi_{\mathcal{S}}$ AND D ($F_{\mathcal{S}}$ DENOTES A CUMULATIVE DISTRIBUTION FUNCTION DERIVED ON THE BASIS OF THE $\mathcal{S}$-KB)

$\mathcal{S}$-KB	Ξ_S	D
Eq. (5)	$\boldsymbol{\chi}_{\text{soft}}$	$\boldsymbol{I}$
Eq. (6)	$F_{\mathcal{S}}(\boldsymbol{\chi}_{\text{soft}})$	$\boldsymbol{I}$
Eq. (7)	$F_{\mathcal{S}}(\boldsymbol{\chi}_{\text{soft}}, \boldsymbol{\chi}_k)$	$\boldsymbol{I} \cup \boldsymbol{I}_k$

TABLE IV
EXAMPLES OF SPACE–TIME PREDICTIONS $\hat{\chi}_k$

BME mode	$\hat{\boldsymbol{\chi}}_{k,\text{mode}} : \max_{\boldsymbol{\chi}_k} f_{\mathcal{K}}^{bc}(\boldsymbol{\chi}_k)$ (9)
BME mean	$\hat{\boldsymbol{\chi}}_{k,\text{mean}} = \int d\boldsymbol{\chi}_k \, \boldsymbol{\chi}_k \, f_{\mathcal{K}}^{bc}(\boldsymbol{\chi}_k)$ (10)

Step 5) The $\mathcal{G}$-based pdf model $f_{\mathcal{G}}$ is revised through application of the operational Bayesian conditionalization (bc) rule to yield the *integration* (or *posterior*) pdf that are consistent with the $\mathcal{S}$-KB available, as follows:

$$f_{\mathcal{K}}^{bc}(\boldsymbol{\chi}_k) = A^{-1} \int_D d\Xi_S(\boldsymbol{\chi}_{\text{soft}}) \, f_{\mathcal{G}}(\boldsymbol{\chi}_{\text{map}}) \tag{8}$$

where $KB = \mathcal{K} = \mathcal{G} \cup \mathcal{S}$, and A is a normalization parameter independent of $\boldsymbol{\chi}_k$. The $f_{\mathcal{K}}^{bc}$ contains all the possible information we can obtain about an atmospheric situation in view of the uncertainty and space–time heterogeneity features of a real-world open system.

Step 6) From (8), we select the appropriate predictions (interpolations), $\hat{\boldsymbol{\chi}}_k$, across space and time, depending on the goals of the study. The BMEmode prediction in (9) of Table IV, for example, represents the most probable TO_3 realization, whereas the BMEmean [see (10)] minimizes the mean squared prediction (interpolation) error. Other forms of interpolation can be derived so that they optimize an objective function. The predicted values $\hat{\boldsymbol{\chi}}_k$ are used to create informative spatiotemporal maps, which can be scientifically interpreted to provide a useful picture of reality and generate science-based decisions.

Step 7) Because of the inherent randomness of the $X(\boldsymbol{p})$ field and the inaccuracies of the physical data, one can use the pdf (8) to obtain an uncertainty assessment associated with $\hat{\boldsymbol{\chi}}_k$. A popular measure of interpolation accuracy is the prediction (interpolation) error standard deviation of $f_{\mathcal{K}}^{bc}$, calculated at each map grid point of the atmospheric domain—see also

(17) below. Other accuracy measures (including confidence intervals and sets) can be also calculated [32].

By way of a summary, the theoretical models of the $\mathcal{G}$-KB in Step 1) above elucidate fundamental principles governing the general behavior of the atmospheric system; however, space–time prediction of the specific behavior of the system usually remains uncertain as implied by the $\mathcal{S}$-KB of Step 3). Beyond the clear significance of acquiring the $\mathcal{G}$– and $\mathcal{S}$-KB, the BME theory quite appropriately emphasizes the importance of a rigorous logical process that allows the adequate *synthesis* of these two KB [Steps 4) and 5)]. Atmospheric data assimilation often involves a series of physical models, usually in the form of partial differential equations (PDEs). These include tracer transport and general circulation models [14], [26], [28]. Physical PDE models can certainly be processed by BME (e.g., see [10], [12], [24], and [33]; see also Section IV). However, because of the different goals of the present study (as outlined in Section I) no physical PDE models were assumed to be part of the $\mathcal{G}$-KB of the situation.

III. Model Application

A. Interpolation Methodology

The SBUV data can offer valuable information on the TO_3 distribution in the atmosphere and are used as a major source of daily stratospheric ozone data. However, the spatial resolution of the SBUV data is inadequate to assess the high spatial resolution variability of TO_3 or stratospheric ozone, since the measurements were obtained only along the subsatellite track [Fig. 1(a)]. Because there is considerable spatiotemporal variability for TO_3 and uncertainty in the SBUV data, it is very difficult to interpolate these data and obtain reasonably accurate analyses of TO_3 in the large region between subsatellite tracks. The BME interpolation approach, however, offers the potential for producing analyses of these data with better representation of the TO_3 variability between subsatellite tracks than conventional interpolation procedures, because it does not use the restrictive modeling assumptions used by conventional techniques, and it can incorporate various kinds of uncertain (soft) data, which are not used in conventional techniques. The BME-based analyses of the TO_3 distribution for the present study will include the following stages.

1) Section III-B: The spatiotemporal variation of TO_3 for July 6, 1988 is modeled as a random field. Instead of using SBUV measurements directly as hard data, however, TOMS data closest to the locations of the SBUV measurement points [Fig. 1(a)] were selected as hard data for the analysis [Fig. 1(b)].
2) Section III-C: Soft information, which relates TO_3 to the tropopause pressure, was generated through the development and application of an empirical physical equation. This kind of empirical correlation is well documented in the atmospheric sciences literature.
3) Section III-D: A conventional interpolation technique was initially used to interpolate the TO_3 in the data gaps between the subsatellite points/SBUV data locations. Values of TO_3 were predicted at all grid nodes [indicated by plus markers in Fig. 1(a)] based only on the TOMS data selected at the SBUV data locations. Then, the BME techniques predicted TO_3 values at all grid nodes by integrating the hard data described in Stage 1) together with the soft information described in Stage 2) above. Two computational BME versions were considered in this section to generate TO_3 values at the interpolation nodes $\boldsymbol{p}_k$ across space–time. The BME1, in which case the $\mathcal{S}$-KB included soft information at the data points $\boldsymbol{p}_i$ (i.e., $\boldsymbol{p}_i \neq \boldsymbol{p}_k$); and the BME2, in which case the $\mathcal{S}$-KB included soft information at the data points $\boldsymbol{p}_i$ as well as the interpolation points $\boldsymbol{p}_k$ themselves.
4) Section III-E: The results obtained from application of the different interpolation techniques in Stage 3) above were compared with the complete set of TOMS measurements in the area defined in Fig. 1(a).

B. Spatial Variation of Total Ozone

In Fig. 3 we show the actual maps of TO_3 generated by using the entire TOMS dataset for the sixth day of the months of January, April, July, and October of 1988 (blank strips indicate small areas where data were not available). In the following, these maps will serve as *reference* maps for comparison purposes. In the context of the $\mathcal{G}$-KB, the TO_3 distribution is represented by the spatiotemporal random field

$$TO_3(\boldsymbol{p}) = \overline{TO_3}(\boldsymbol{p}) + X(\boldsymbol{p}) \tag{11}$$

where $\overline{TO_3}(\boldsymbol{p})$ is the space–time trend of TO_3, and $X(\boldsymbol{p})$ is a zero-mean spatially homogeneous/temporally stationary random field of ozone fluctuations. The $\overline{TO_3}(\boldsymbol{p})$ is determined by applying a moving window averaging to the TO_3 data with exponential filter. Given TO_3 and $\overline{TO_3}(\boldsymbol{p})$ at each data point, the residual ozone $X(\boldsymbol{p})$ is calculated from (11). Moreover, on the basis of background knowledge, a system of theoretical covariance models with nested exponential and Gaussian components was assumed to be part of the $\mathcal{G}$-KB about the residual ozone $X(\boldsymbol{p})$ distribution. Members of this system belong to the general covariance functional

$$c_x(r_{ij},\tau_{ij}) = \Phi[c_d, e^{(r_{ij},r_{ij}^2,\tau_{ij},\tau_{ij}^2;a_{r_d},a_{\tau_d})}], \qquad d=1,2. \tag{12}$$

The $\Phi[\cdot]$ denotes a space–time nonseparable functional (some examples are given in Table V); $r_{ij} = |\boldsymbol{s}_i - \boldsymbol{s}_j|$ is the spatial distance between any pair of locations in the atmosphere, and $\tau_{ij} = |t_i - t_j|$ is the corresponding temporal distance; the c_d denote sill coefficients and the a_{rd}, $a_{\tau d}$ ($d = 1, 2$) denote correlation range coefficients. As is shown in Table V, various covariance models of the form (12) are fitted to the experimental covariances obtained from the $\boldsymbol{\chi}_{\text{hard}}$ data over the United States during different time periods. The space–time covariances of the residual ozone $X(\boldsymbol{p})$ distribution for the months of January, April, July, and October of 1988 are plotted in Fig. 4(a)–(d). These plots offer useful information about the space–time correlation patterns of $X(\boldsymbol{p})$: the asymptotic shapes of the covariance models at large space–time distances imply a spatially homogeneous/temporally stationary variation of $X(\boldsymbol{p})$; the choice of a model component with a parabolic behavior at the origin reflects a naturally smooth variation of ozone distribution along certain

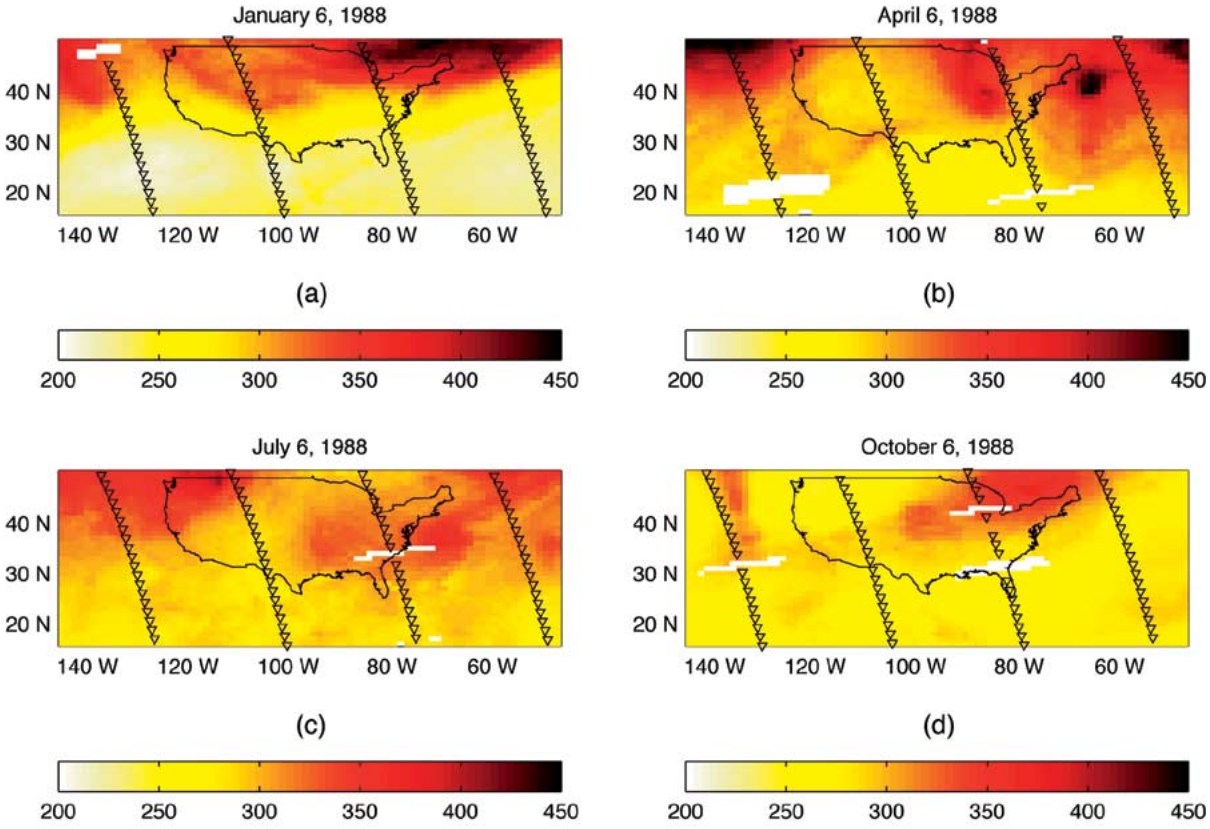

Fig. 3. Actual distributions of TO_3 (in DU) obtained from the TOMS instrument, as well as the actual locations of the SBUV measurements (shown in triangles) on (a) January 6, (b) April 6, (c) July 6, and (d) October 6, 1988.

TABLE V
THEORETICAL SPACE–TIME COVARIANCE MODELS OF THE FORM OF (12). SILL UNITS ARE IN DU^2. SPATIAL RANGES ARE EXPRESSED IN DECIMAL DEGREES, AND TEMPORAL RANGES IN DAYS

Month in 1988	**Space-time models**	c_1 (DU^2)	c_2 (DU^2)	a_{r1} (DD)	$a_{\tau 1}$ $(days)$	a_{r2} (DD)	$a_{\tau 2}$ $(days)$
January	$c_x(r_{ij},\tau_{ij}) = c_1 e^{-3r_{ij}^2/a_{r1}^2} e^{-3\tau_{ij}/a_{\tau 1}} + c_2 e^{-3r_{ij}/a_{r2}} e^{-3\tau_{ij}^2/a_{\tau 2}^2}$	0.7	0.3	12	2	17.5	4
April	$c_x(r_{ij},\tau_{ij}) = c_1 e^{-3r_{ij}^2/a_{r1}^2} e^{-3\tau_{ij}/a_{\tau 1}} + c_2 e^{-3r_{ij}/a_{r2}} e^{-3\tau_{ij}^2/a_{\tau 2}^2}$	0.65	0.35	14	2	25	2
July	$c_x(r_{ij},\tau_{ij}) = c_1 e^{-3r_{ij}/a_{r1}} e^{-3\tau_{ij}/a_{\tau 1}} + c_2 e^{-3r_{ij}^2/a_{r2}^2} e^{-3\tau_{ij}^2/a_{\tau 2}^2}$	0.35	0.65	7	2	12	3
October	$c_x(r_{ij},\tau_{ij}) = c_1 e^{-3r_{ij}^2/a_{r1}^2} e^{-3\tau_{ij}^2/a_{\tau 1}^2} + c_2 e^{-3r_{ij}^2/a_{r2}^2} e^{-3\tau_{ij}/a_{\tau 2}}$	0.7	0.3	11	2.5	15	2

directions in the stratosphere, whereas the behavior of the exponential component at the origin accounts for the contribution of a less smooth process, etc. The components of the covariance models (12) have physical significance. In the case of the covariance model of July 1998 (Table V), for example, the exponential component represents processes with a rather high spatial variability over a range of about 7 DD (decimal degrees), approximately 777 km on the earth's surface, while the Gaussian

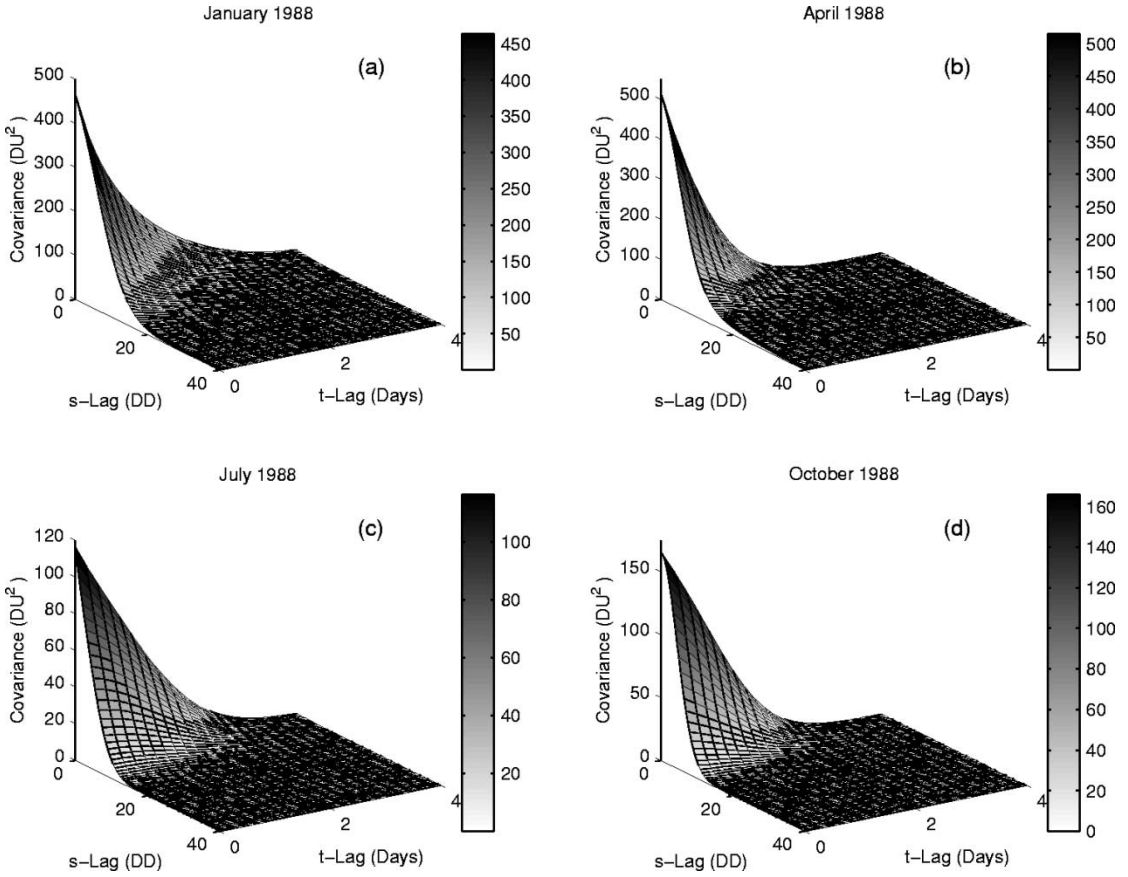

Fig. 4. TO_3 spatiotemporal covariance (in DU^2) models based on the corresponding experimental covariance data extracted from the TOMS datasets for the month of (a) January, (b) April, (c) July, and (d) October, 1988. The spatial lag units are decimal degrees.

component represents smoother processes with a longer range of about 12 DD (approximately 1332 km on the earth's surface). Also, since the covariances of January and April experience considerably larger sills than these of July and October, one may expect larger interpolation errors in the former months—on average [see also Fig. 7(b) and (c) and 12(a)–(c)].

We used TOMS version 7 TO_3, which has, at most, a 2% to 3% error due to such factors as not accounting for the scan-angle dependence and the effect of aerosols properly when deriving the TO_3 from the TOMS measurements. The TOMS data at the SBUV measurement locations were used as a first-order approximation of "hard" data to determine if the BME interpolation procedure could reproduce the ozone variability between the SBUV measurement locations (i.e., essentially the satellites track at the surface) with significantly better accuracy than the conventional interpolation procedures presently being used. It should be noted that the TOMS footprint has a spatial resolution of 50 km at nadir, and the spatial resolution varies with latitude and viewing angle. For this study, we used the gridded TOMS data (Nimbus 7, version 7, level 3 gridded ozone), which has a $1 \times 1.125^\circ$ resolution corresponding to a 50-km spatial resolution at nadir.

C. Soft (Secondary) Information

The soft data used for this paper are the tropopause pressure data P_t, which are model-generated data that were created by the National Center for Atmospheric Prediction (NCEP) and which incorporates observed upper air data. The NCEP tropopause pressure was derived using a World Meteorological Organization 2 °K/km definition. Empirical correlations between total ozone and tropopause pressure have been documented in several studies (e.g., [31] and [35]). It is often assumed that changes in the dynamic structure of the atmosphere, as reflected in P_t, are an immediate driving force for TO_3 fluctuations [1]. In particular, when P_t increases, the height of the tropopause, H_t, decreases and the depth of the stratosphere becomes larger, and thus includes more ozone (i.e., has a larger value for TO_3). Let ΔO_3 be the difference between the average O_3 concentration per unit height in the stratosphere, $\overline{O_{3,\mathrm{st}}}$, and the average O_3 concentration per unit height in the troposphere, $\overline{O_{3,\mathrm{Tr}}}$, i.e., $\Delta O_3 = \overline{O_{3,\mathrm{st}}} - \overline{O_{3,\mathrm{Tr}}}$. Assuming that ΔO_3 remains approximately constant for a small change in H_t, δH_t, the resulting change in TO_3, δTO_3, can be given by $\delta TO_3/\delta H_t = -\Delta O_3$ (i.e., an increase in H_t results in a linear decrease in TO_3). This equation approximates a constant rate of increase of TO_3. Integrating from some initial state ($TO_{3,0}$ at $H_{t,0}$), we get $TO_3 = TO_{3,0} - a(H_t - H_{t,0})$, where TO_3 is measured in DU, H_t and $H_{t,0}$ are measured in *meters*, and α is the linear rate of decrease of TO_3. Consider the phenomenological law [38], $P = P_0 e^{-H/H_0}$, where P is pressure, P_0 is the surface pressure, H is the height, and H_0 is the scale height of the atmosphere (approximately 7 km). Rearranging terms, the following formula-

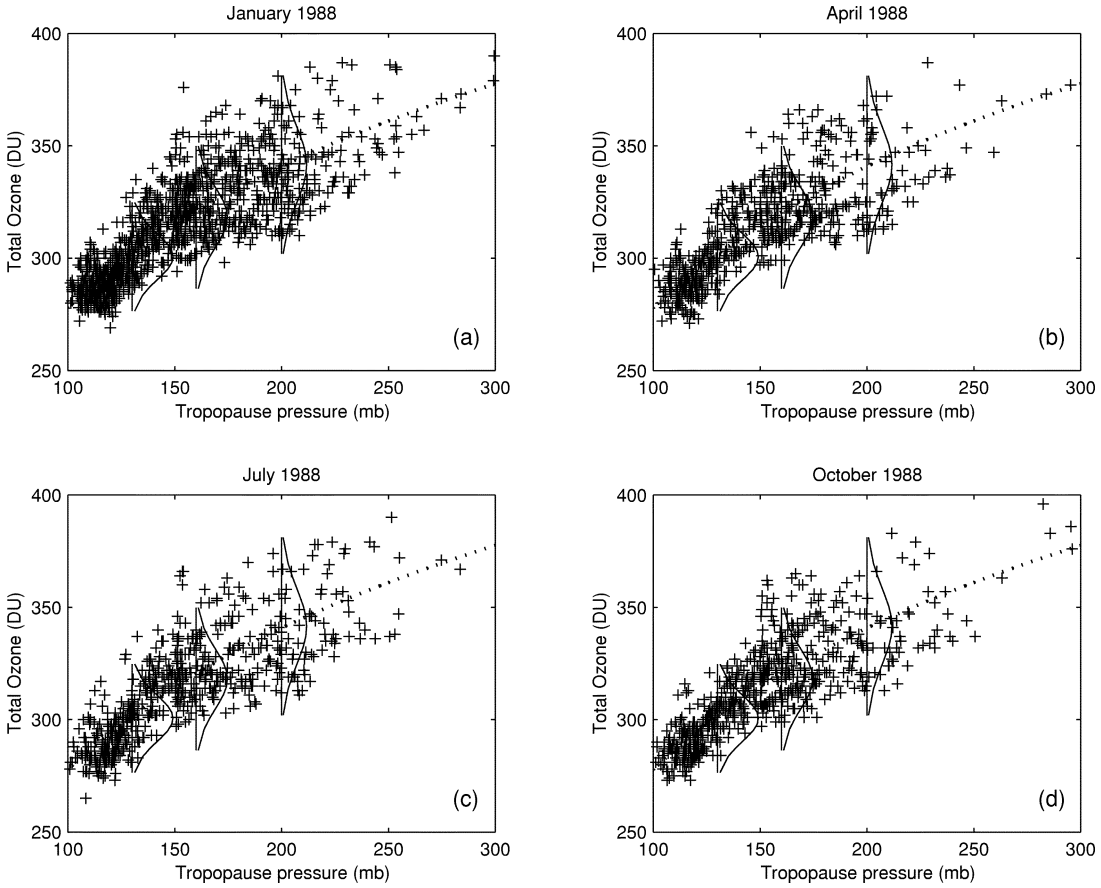

Fig. 5. Scatter plots of TO_3 measurements versus tropopause pressure. A physical equation (shown in dotted line) is fitted to the data for the month of (a) January, (b) April, (c) July, and (d) October 1988, from which the corresponding soft pdfs $f_S(\boldsymbol{\chi}_{\text{soft}})$ can be derived. Three of these pdfs are shown each month for illustration.

tion—which relates the total ozone (TO_3) with the tropopause pressure (P_t)—is obtained

$$TO_3(\boldsymbol{s}) = a_0 + a_1 \log P_t(\boldsymbol{s}) \tag{13}$$

where $a_0 = TO_{3,0} + aH_{t,0} - aH_0 \log P_0$ and $a_1 = aH_0$, which can be estimated by experimental data fitting. The parameters a_0 and a_1 are viewed as random variables representing such factors as uncertainties due to fluctuations in ΔO_3, and perturbations in the atmosphere. For each value of P_t, a soft pdf is derived that represents the probabilistic distribution of TO_3 values, which provides the physical basis for producing the soft information that is used by BME analysis. The use of (13) in TO_3 prediction is further supported by the fact that several authors have argued that the tropopause pressure model set up could perform better than that using other atmospheric variables, e.g., the North Atlantic oscillation index [1].

Fig. 5(a)–(d) depicts typical scatter plots of TO_3 versus P_t at concurrent points (shown by plus markers) during four different months (January, April, July, and October). At each scatter plot, the dotted line is derived using (13), where a_0 and a_1 are the best fit to the experimental data. The dotted line represents the general behavior of the relationship between TO_3 and P_t. However, due to the stochastic nature of (13), each value of P_t corresponds to an uncertain value of TO_3. Equation (13) is based on an approximation of the true relationship between pressure and height, which assumes that the atmospheric temperature is constant through the depth of the atmosphere, when in reality it varies with height. Nevertheless, the consideration of the parameters a_0 and a_1 as random variables (so that (13) is properly adjusted to fit experimental data) allows us to generate useful soft (probabilistic) information representing the uncertainty in the $\boldsymbol{\chi}_{\text{soft}}$-values of TO_3, as follows. First, the data are divided into classes of contiguous nonoverlapping intervals of P_t. Based on the data, we considered 42 equally wide classes of size 5 mb. Then, for each class of P_t-values, the experimental mean and variance of corresponding TO_3-values are derived. The means and variances define a unique Gaussian probability distribution of the P_t-values whose pdf we define as the $f_S(\boldsymbol{\chi}_{\text{soft}})$ for each class. Some of these densities that are associated with three selected classes are given in Fig. 5(a)–(d) for illustration. Based on this procedure, a probability datum for TO_3 can be assigned to each P_t data point, providing the uncertainty in the TO_3-values across space. The geographical locations where probability data $f_S(\boldsymbol{\chi}_{\text{soft}})$ were generated are shown as circles in Fig. 1(b). As already mentioned, one can find in the literature several studies on TO_3- P_t correlation. One of the earlier ones using satellite data is due to Schubert and Munteanu [31]; a more recent one is due to Steinbrecht *et al.* [35]. Future BME–based works will rely on an improved physical relationship of pressure versus height, by incorporating additional soft information sources (e.g., potential vorticity data, and temporal information in the database), etc. Moreover, future

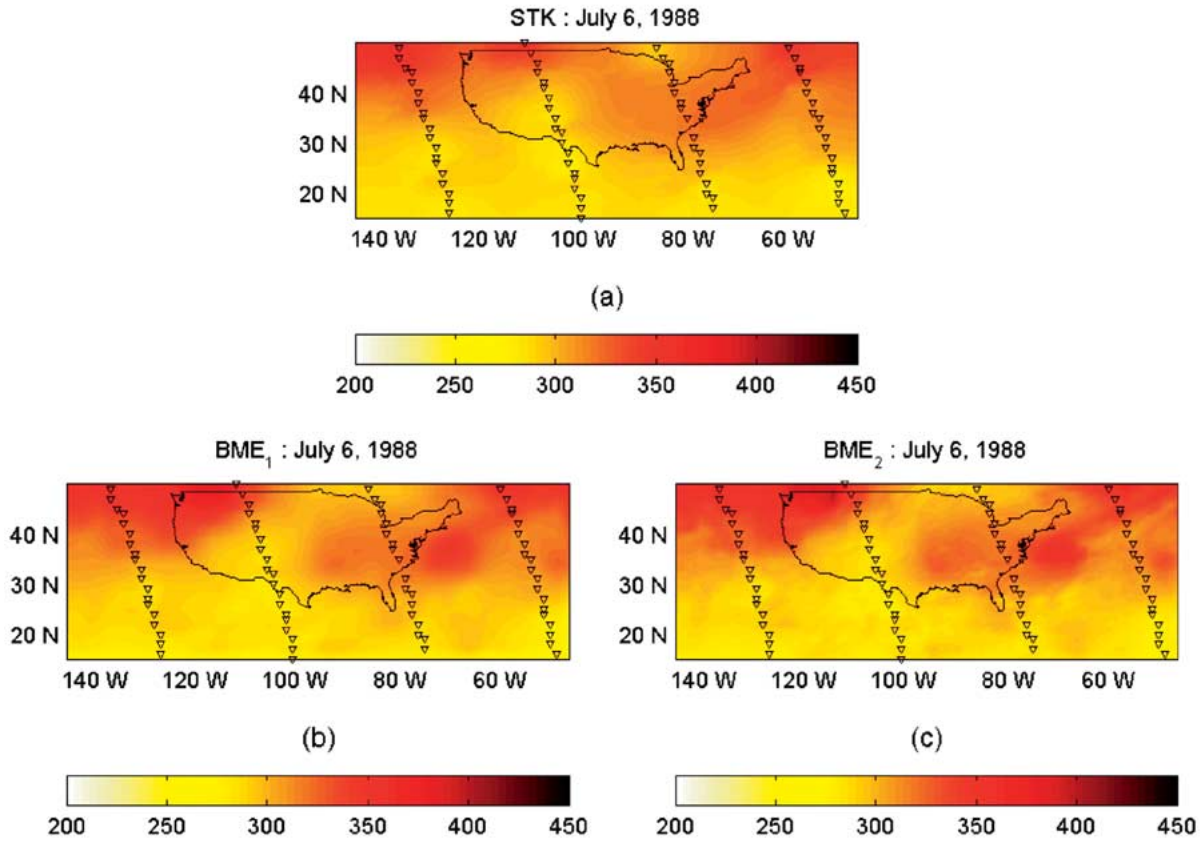

Fig. 6. TO_3 maps (in DU) for July 6, 1988, using (a) STK, (b) BME1, and (c) BME2. The triangles designate hard-data locations (TOMS data closest to the SBUV measurements on that day) used by all three techniques. The locations of the soft data are depicted by circles in Fig. 1(b). Additional soft data used by BME2 in (c) are located at the interpolation points designated by plus markers in Fig. 1(a).

works would take into consideration the empirical laws relating ozone and a wide range of meteorological parameters, including lower stratospheric temperature and potential vorticity (as documented, for example, in [23] and [29]).

D. Interpolation Methodologies

For numerical comparison purposes, we considered two different methodologies of space–time modeling and interpolation:

- *Methodology 1*, which relies on inductive principles and forms the basis of the conventional (regression-type) techniques (see Wiener–Kolmogorov filter, kriging, neural networks, etc.);
- *Methodology 2*, which employs teleologic/integration principles and underlies the MSG techniques (see Section II-A).

In the context of Methodology 1, we assumed that the site-specific KB, $\mathcal{S}$, consists of the hard TO_3 dataset derived from TOMS data closest to the SBUV measurement points across space–time. In this case, the spatiotemporal geostatistical kriging technique (STK) [7] was used to interpolate TO_3 in the remaining area [i.e., at all points shown with plus markers in Fig. 1(a)] on July 6, 1988. The corresponding covariance model of Table V (July 1988) was implemented to represent composite space–time correlations. At each grid node $\boldsymbol{p}_k = (\boldsymbol{s}_k, t_k)$, the STK assumes a linear interpolator of the form

$$\hat{\chi}_k = \boldsymbol{\xi}^T \boldsymbol{\chi} \tag{14}$$

where $\boldsymbol{\xi}$ is the vector of interpolation weights calculated from the interpolation system, and $\boldsymbol{\chi}$ is a vector that includes the space–time TO_3 hard data used in calculating the TO_3 prediction $\hat{\chi}_k$ at a grid node $\boldsymbol{p}_k = (\boldsymbol{s}_k, t_k)$. The $\boldsymbol{\chi}_{\text{hard}}$ includes TO_3 data at time t_k as well as at other time instants. The corresponding STK-based map of TO_3 distribution is shown in Fig. 6(a). The STK interpolation error standard deviation of the TO_3 interpolation at any point $\boldsymbol{p}_k$ is calculated as

$$\sigma_e(\boldsymbol{p}_k) = \left[\sigma_x^2 - \boldsymbol{c}_x^{*T} \boldsymbol{c}_x^{-1} \boldsymbol{c}_x^*\right]^{1/2} \tag{15}$$

where σ_x^2 is the variance of the TO_3 fluctuations, $\boldsymbol{c}_x$ is the covariance matrix between the data points themselves, and $\boldsymbol{c}_x^*$ is the covariance matrix between the data and the interpolation points. The σ_e-map is plotted in Fig. 7(a). One should note that, as was mentioned in Section II-B, the conventional interpolation technique [(14) and (15)] can be derived as a special case of the general BME theory under the restrictive conditions on the $\mathcal{S}$-KB described above.

In addition to the hard dataset above, the techniques of Methodology 2 process site-specific soft information (Section III-C) to predict TO_3 in the SBUV data gaps. The BME technique, in particular, was used to interpolate TO_3 in the data gap locations. As for STK, for this paper, TOMS data closest to the location of the SBUV measurement points in space–time were used as hard data for the analysis. The basic interpolation

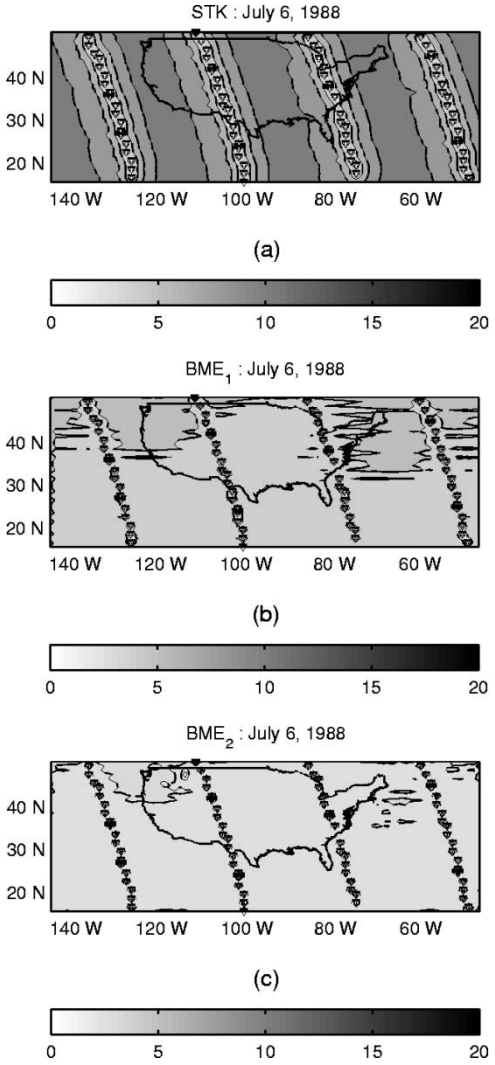

Fig. 7. TO_3 interpolation error standard deviations (in DU) associated with the maps in Fig. 6 for (a) STK, (b) BME1, and (c) BME2.

equation for the BMEmean (which accounts for both hard and soft databases) is [10]

$$c_{kk}^{-1}(\hat{\chi}_k-\overline{x_k})+\sum_{i=1}^{m_h}c_{ik}^{-1}(\chi_i-\overline{x_i})+\sum_{i=m_h+1}^{m}c_{ik}^{-1}[\theta_i(\hat{\chi}_k)-\overline{x_i}]=0 \quad (16)$$

where

$$\theta_i(\hat{\chi}_k)=\left[\int_D d\Xi_S\, e^{\boldsymbol{\mu}^T\boldsymbol{g}|_{\chi_k=\hat{\chi}_k}}\right]^{-1}\int_D d\Xi_S\,\chi_i\, e^{\boldsymbol{\mu}^T\boldsymbol{g}|_{\chi_k=\hat{\chi}_k}}$$

and $d\Xi_S = f_S\, d\boldsymbol{\chi}_{\text{soft}}$, in this case; the c_{ik}^{-1} and c_{kk}^{-1} are the ikth and kth elements, respectively, of the inverse of the matrix with elements the covariances between data and estimation points as well as the covariances between the data points themselves. It is instructive to compare (14) and (16). While in (14) the interpolator $\hat{\chi}_k$ is restricted to a linear combination of the data, in (16) the interpolator $\hat{\chi}_k$ is nonlinear, in general, thus demonstrating the more powerful theory underlying the BME interpolator. This is a considerable advantage of Methodology 2 over Methodology 1. The resulting BMEmean maps are plotted in Fig. 6(b) and (c). In the Fig. 6(a), the soft dataset referred to space–time points $\boldsymbol{p}_i$ [depicted with circles in Fig. 1(b)] different than the interpolation points $\boldsymbol{p}_k$ [designated with plus markers in Fig. 1(a)] (BME1), whereas in Fig. 6(b), additional soft data were assumed available at the interpolation points $\boldsymbol{p}_k$, as well (BME2). In particular, to demonstrate the improvements gained by using BME2 when soft data are available at the interpolation nodes $\boldsymbol{p}_k$, we assumed that a soft datum in the form of a TO_3 probability distribution was available at the interpolation node $\boldsymbol{p}_k$ itself (the mean value of the soft datum was selected to vary randomly within an interval that included the TOMS datum at the same location, i.e., at any given interpolation node only one soft datum was added to the previous dataset). Although this soft datum was intentionally contaminated by error, nevertheless BME2 was able to make optimal use of this limited information and generate improved results (see Section III-E). The associated maps of interpolation error standard deviation values at any grid node $\boldsymbol{p}_k$, which is obtained using the expression

$$\sigma_{\mathcal{K}}(p_k)=\left[\int d\chi_k\,(\chi_k-\overline{x_k})^2\, f_{\mathcal{K}}^{bc}(\chi_k)\right]^{1/2} \quad (17)$$

are shown in Fig. 7(b) and (c) (BME1 and BME2, respectively; the mean value of the TO_3 fluctuation at the interpolation point $\boldsymbol{p}_k$ is $\overline{x_k}=0$, in this case). The errors in Fig. 7(b) and (c) are smaller than the STK errors in Fig. 7(a) (in the latter figure, the errors are small only close to the hard-data points and increase quickly as one moves away from these points). It may be possible that STK be simply modified to also take into account some information based on (13). Despite the fact that such modifications are rather ad hoc schemes (e.g., they are not based on a general methodological framework with sound theoretical support as do the BME techniques of Methodology 2), the resulting interpolator will be theoretically inferior to BME (because of the linearity restriction, the normality limitation, etc. [4]). Also, the reader is cautioned that σ_e is independent of data values and, as a consequence, has been the subject of some criticism [22]. The $\sigma_{\mathcal{K}}$, on the other hand, depends on the specific dataset considered and offers an adequate interpolation error assessment when the shape of the pdf is not very complicated. In the case of an underlying Gaussian law, the probability that χ_k lies in the interval $\hat{\chi}_{k,\text{mean}}\pm 1.96\,\sigma_{\mathcal{K}}$ is 95%. In some other cases where $f_{\mathcal{K}}^{bc}$ has a complicated shape, a realistic assessment of the analysis error is achieved using BME confidence sets [32].

E. Mapping Results

Comparison of the maps in Fig. 6 with the map in Fig. 3(c) (TOMS values in July 6, 1988) shows that BME has certain important advantages that make it a better technique to study ozone's distribution in the atmosphere. Indeed, the STK map of Fig. 6(a) clearly misrepresents the TO_3 variation in certain areas and shows poor accuracy away from the hard-data points. On the other hand, the maps of Fig. 6(b) and (c) (BME1 and BME2, respectively) offer a much more realistic representation of the TO_3 variation, particularly in the regions off the east coast and at

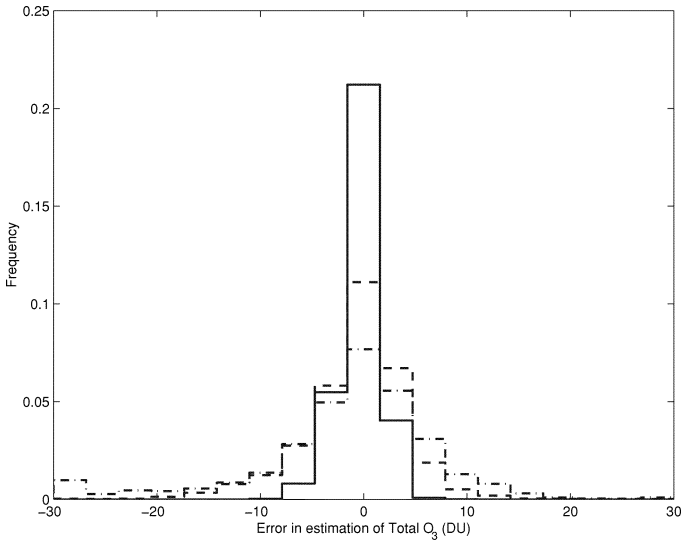

Fig. 8. Frequency distributions of spatiotemporal TO_3 interpolation errors obtained by (dashed–dotted line) STK, (dashed line) BME1, and (plain line) BME2.

the west coast, leading to greater comparability with the TOMS values. It is worth noticing that the BME2 map [Fig. 6(c)] is an improvement over the BME1 map [Fig. 6(b)], which demonstrates the importance of using soft data at the interpolation points, whenever available. Moreover, interpolation error standard deviation offers a method to examine the level of improvement in the resulting analyses. Again, the corresponding maps indicate that the BME techniques [Fig. 7(b) and (c)] offer a significant improvement over the STK technique [Fig. 7(a)]. In conventional interpolation, errors σ_e are rather small along the satellite paths but increase considerably away from the paths, reaching their maximum values along the axis between the subsatellite tracks. On the other hand, the BME error maps ($\sigma_{\mathcal{K}}$) depict an error distribution that does not increase dramatically away from subsatellite tracks.

In order to further compare the accuracy of the STK technique of Methodology 1 versus the accuracy of the BME techniques of Methodology 2, we calculated the differences between the predicted TO_3 values on July 6, 1988 [Fig. 6(a)–(c)] and the reference values [Fig. 3(c)] at all data points at which TO_3 values are available from TOMS. The histograms of the interpolation errors are shown in Fig. 8. Both BME techniques have sharper peaks than the STK technique around zero interpolation error, which implies that by integrating soft physical information the BME1 and BME2 produced more accurate TO_3 interpolations at a much higher frequency than the STK. In addition, the mean square error (MSE), i.e., the average of the squared interpolation errors, drops from 110 DU^2 (STK) down to 26.53 DU^2 (BME1) and 3.62 DU^2 (BME2), corresponding to improvements of 75.9% and 96.71%, respectively. These improvements confirm what was expected from the corresponding maps of interpolation errors (Fig. 7). Another measure of error, normally referred to as the bias, is the mean error (ME), i.e., the average of interpolation errors. The ME is equal to -1.96 DU (STK), indicating a small underprediction of the TO_3, whereas the ME value drops to -0.79 DU (BME1) and -0.28 (BME2),

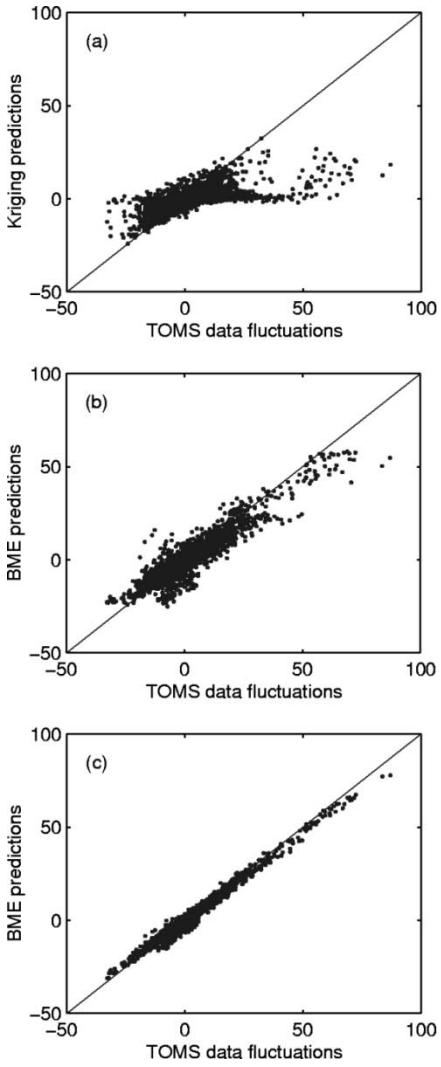

Fig. 9. Scattergram of the TOMS data fluctuations versus the corresponding interpolated values (detrended: in DU) for July 6, 1988 using (a) STK, (b) BME1, and (c) BME2 (the perfect line is also shown for comparison).

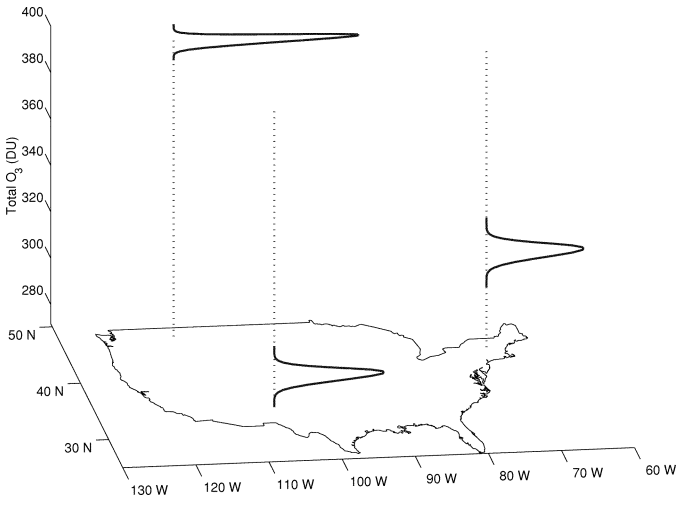

Fig. 10. Integration (posterior) pdfs $f^{bc}_{\mathcal{K}}$ of possible TO_3 values (in DU) at three locations over the United States using BME2 interpolation results for July 6, 1988.

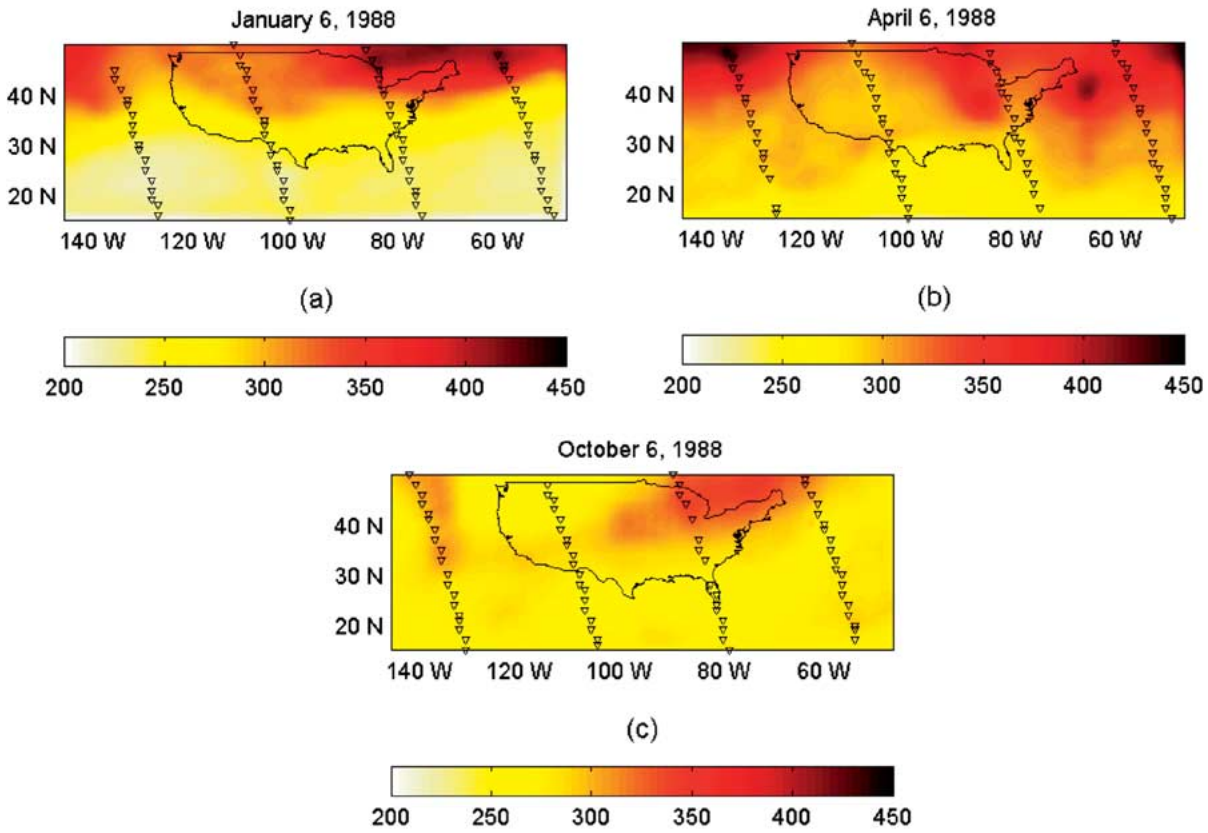

Fig. 11. Seasonal comparison maps of BME1 interpolations of spatiotemporal TO_3 distributions (in DU) for (a) January 6, (b) April 6, and (c) October 6, 1988. The hard-data locations for each month are shown as triangles on the maps. The soft-data locations are depicted by circles in Fig. 1(b).

indicating an improvement of 59.9% and 85.8%, respectively. The corresponding mean absolute errors (MAE) are 6.44 DU (STK), 3.59 DU (BME1), and 1.38 DU (BME2), i.e., MAE decreases of 44.36% (BME1) and 78.53% (BME2) relative to STK, which show a much better correlation for the techniques of Methodology 2 than for these of Methodology 1.

Some important comparisons for the National Aeronautics and Space Administration's purposes are provided by the corresponding scattergram of TOMS data fluctuations versus the interpolations of the same fluctuations obtained by the techniques of Methodologies 1 and 2. The scattergram of STK does not show a good fit [Fig. 9(a)]; the corresponding correlation coefficient is equal to 0.66. On the other hand, the scattergrams of BME1 and BME2 show excellent fits [Fig. 9(b) and (c)]; the correlation coefficients are equal to 0.923 (BME1) and 0.990 (BME2), which is an almost perfect fit. Thus, there is a correlation improvement of 41% to 50% in favor of Methodology 2 versus Methodology 1. Moreover, as was mentioned in a preceding section, the BME techniques of Methodology 2 can generate the complete pdf ($f_{\mathcal{K}}^{bc}$) of the possible TO_3 values (in DU) at each point across space–time. These pdfs emerge from the stochastic blending of the information contained in the general and site-specific KB. For illustration, three such pdfs are plotted in Fig. 10 for July 6, 1988. Note the considerable spatial variation of the TO_3 mean values of the three pdfs (the selected pdfs are symmetric, mainly due to the fact that they are the outcome of an integration process involving the general KB-based model $f_{\mathcal{G}}$ and the site-specific models $f_{\mathcal{S}}$ [Fig. 5(c)], which were assumed to be symmetric as well; however, in general, a TO_3 model $f_{\mathcal{K}}^{bc}$ can have any shape). Most conventional space–time techniques (including the ones of Methodology 1) cannot produce this kind of spatiotemporal pdf.

Fig. 11(a)–(c) display the BME1 interpolation maps for the sixth day of the months of January, April, and October (1988). For illustration purposes, in this numerical experiment we assumed that no soft data existed at the intorpolation points $\boldsymbol{p}_k$ themselves, although soft information was available at other (neighboring) points $\boldsymbol{p}_i \neq \boldsymbol{p}_k$. Hence, our analysis made use of the BME1 technique in this case. As before, the interpolation maps provide a realistic representation of the reference TOMS maps of Fig. 3(a), (b), and (d). The corresponding BME1 interpolation error maps for the sixth day of January, April, and October (1988) are shown in Fig. 12(a)–(c). Note the following feature of these maps: The clear differences in the spatial distributions of the errors between the months of January, April, and October may be attributed to 1) the varying locations and quality of the soft data during these months as well as 2) the behavior of the corresponding space–time covariances. More specifically, at the set of points characterized by large P_t values the variances of the soft $f_{\mathcal{S}}$-pdfs are larger than at the set of points with smaller P_t values (see Fig. 5), thus yielding larger interpolation errors at the former set of points. The soft data are obtained along the latitude which explains the strips of lower errors surrounding these data in Fig. 12(a) and (b). Soft-data quality improved from

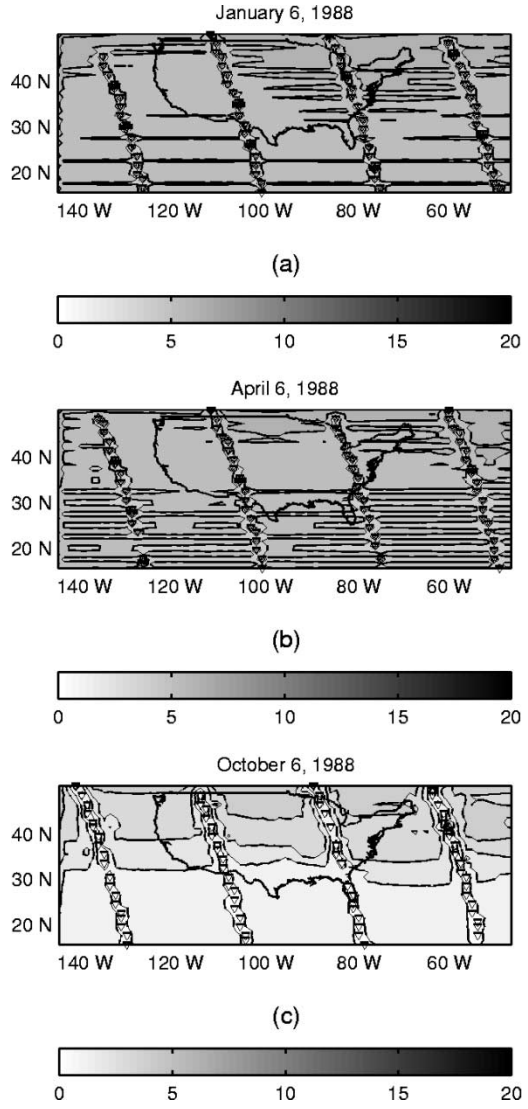

Fig. 12. BME1 interpolation error standard deviations (in DU) associated with the TO_3 maps of Fig. 11 on (a) January 6, (b) April 6, and (c) October 6, 1988.

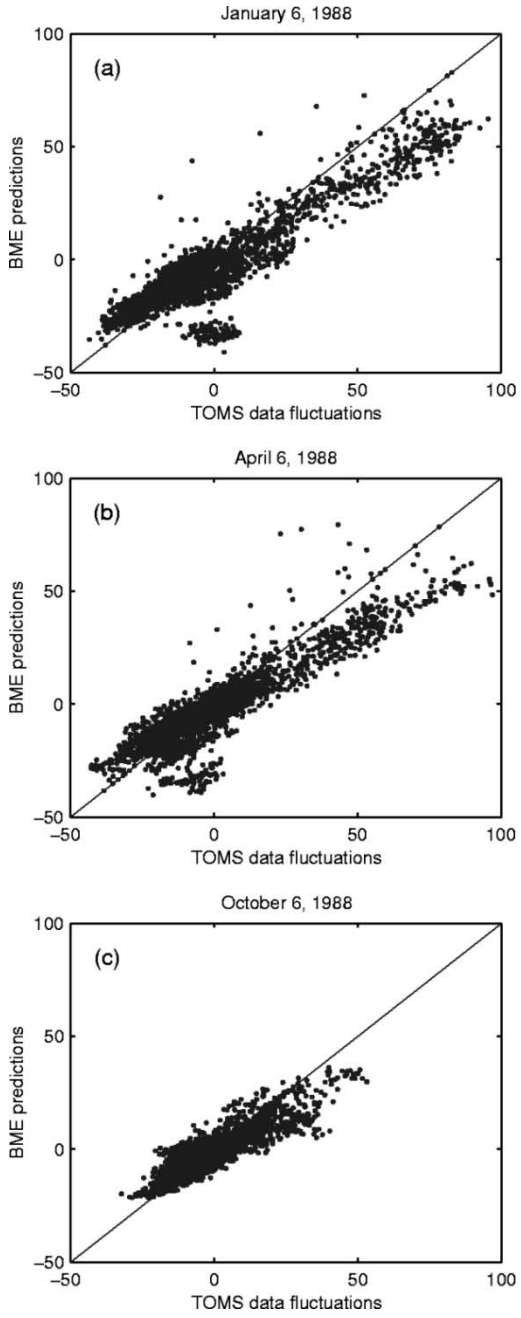

Fig. 13. Scattergram of TOMS data fluctuations versus BME1 interpolations (in DU) for (a) January 6, (b) April 6, and (c) October 6, 1988 (the perfect line is also shown).

north to south during October, leading to the north–south reduced error trend in the map of Fig. 12(c). The October covariance model [Fig. 4(c)] has a smaller sill (about 150 DU^2) than the January and April models (Fig. 4(a) and (b); the sills are over 400 DU^2), which contributed to smaller interpolation errors in October than in the other two months, etc. The scatterplots of the reference TOMS data fluctuations versus the BME1 interpolations are plotted in Fig. 13(a)–(c). Clearly, they all show very good fits: the correlation coefficient are equal to 0.908 (January 6, 1988), 0.906 (April 6, 1988), and 0.882 (October 6, 1988).

To gain some insight about the daily variation of the spatial TO_3 distribution, Fig. 14(a)–(d) shows the reference TOMS maps for four successive days (July 7–10, 1988). Note the varying hard-data locations along the satellite path at different days (due to satellite's movement around the earth). To optimize the outcome of our analysis, in this numerical experiment we assumed that soft data existed at the interpolation points $\boldsymbol{p}_k$ themselves, in addition to the data points $\boldsymbol{p}_i$. This allowed us to implement the BME2 technique. In Fig. 15(a)–(d), we show the corresponding BME2 interpolation maps of TO_3 during the same four days. Two points should be noted. First, these maps accurately detect all major space–time features of the reference maps (hot spots, trends, etc.). Second, the numerical accuracy of the BME2 maps is verified by the corresponding scattergrams of the reference TOMS data fluctuations versus the BME2 interpolations [Fig. 16(a)–(d)] which, indeed, show excellent fits. We conclude our numerical experiments by noting that BME-generated maps such as the above are valuable tools in the dynamic monitoring of ozone's distribution in the atmosphere, which has considerable financial, social, ecological, and human health implications.

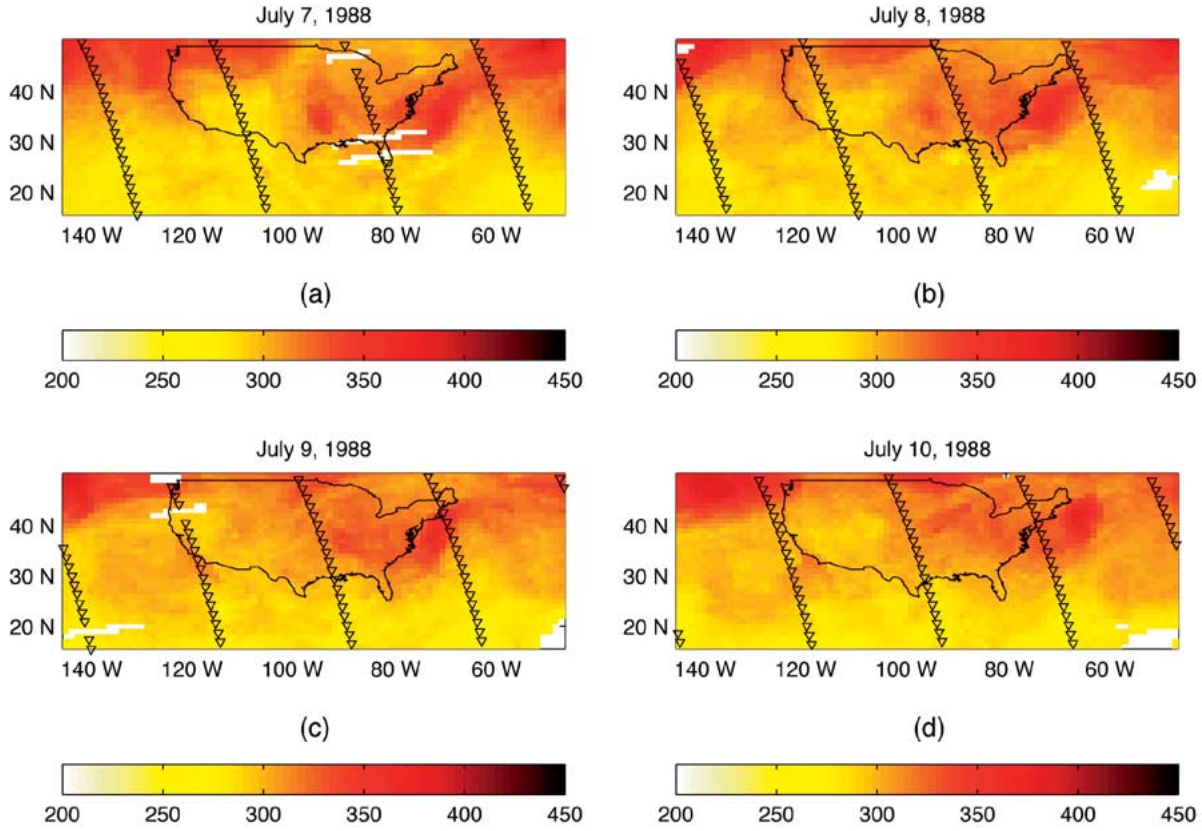

Fig. 14. Reference distributions of TO_3 (in DU) obtained from the TOMS instrument, and locations of the SBUV measurements (triangles) for four consecutive days in 1988: (a) July 7, (b) July 8, (c) July 9, and (d) July 10.

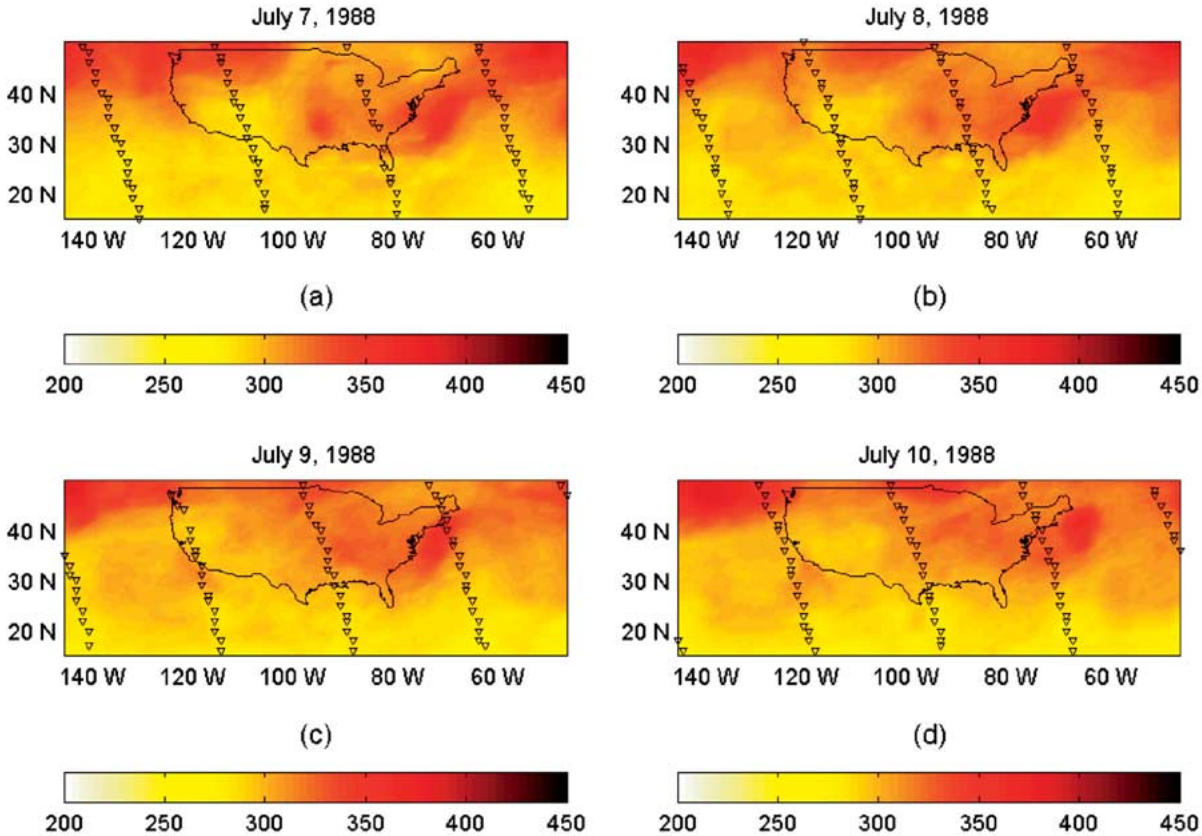

Fig. 15. BME2 interpolation maps of TO_3 (in DU) for (a) July 7, (b) July 8, (c) July 9, and (d) July 10, 1988. Hard-data locations for each day are shown as triangles on the maps. Soft-data locations are depicted by circles in Fig. 1(b). Additional soft data at the interpolation points are denoted by plus markers in Fig. 1(a).

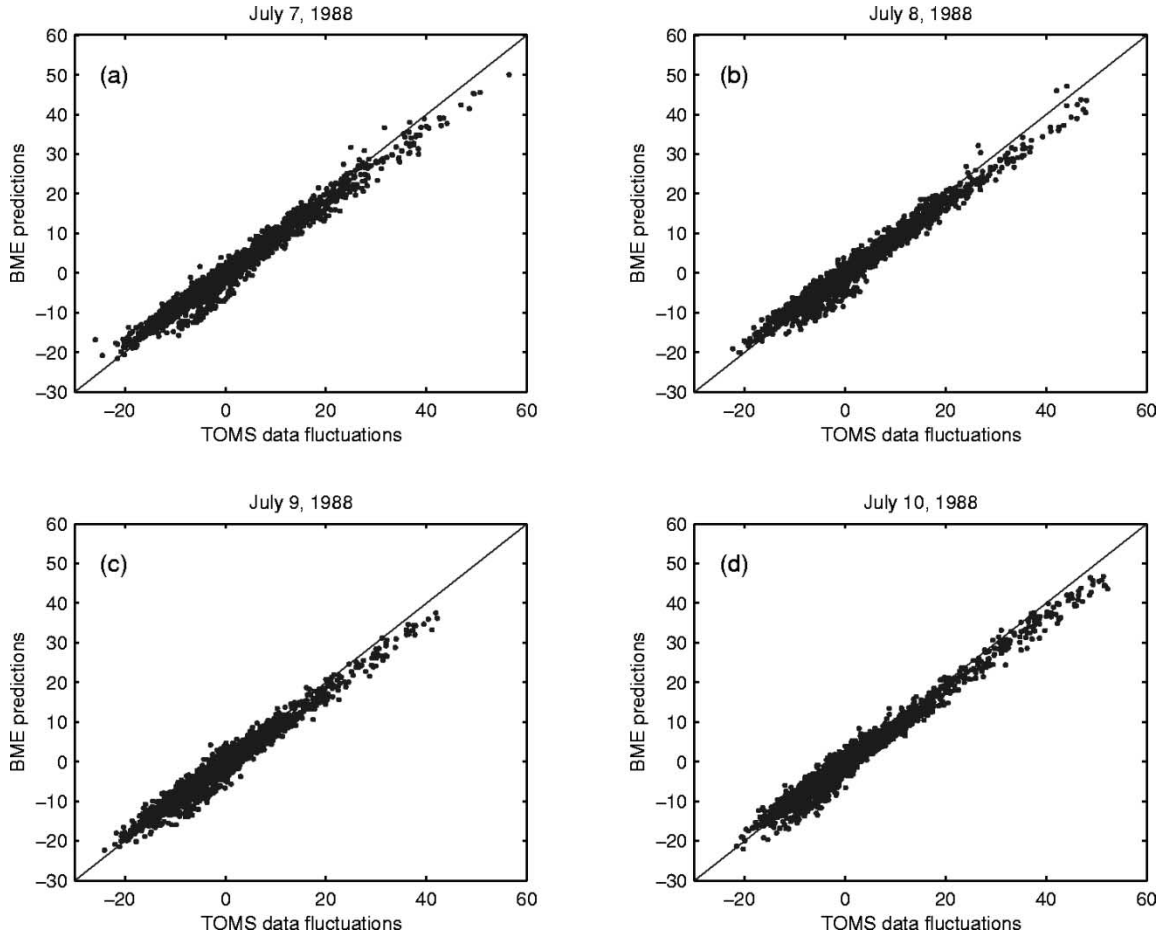

Fig. 16. Scattergram of TOMS data fluctuations versus BME2 interpolations (in DU) for (a) July 7, (b) July 8, (c) July 9, and (d) July 10, 1988 (the perfect correlation line is also shown for comparison).

IV. Discussion and Conclusion

We demonstrated the usefulness and practicality of the BME techniques of MSG to integrate data from various information sources (different instruments, empirical laws, uncertain measurements, etc.) and generate accurate and informative maps of TO_3 variation in the atmosphere. The BME techniques are theoretically powerful (nonlinear/non-Gaussian) schemes that can integrate sparse data obtained at the locations of the SBUV measurements with physical knowledge bases that include the covariance functions (accounting for the variability of ozone values away from the Nimbus 7 satellite path), as well as soft data obtained from the TO_3-tropopause pressure analysis involving empirical physical equations. Accounting for soft data is critical, since it provides a means to incorporate information from the uncertain ozone profile collected by SBUV instruments. Such soft information is rigorously incorporated by the BME techniques, thus yielding more accurate maps of TO_3 than STK. In particular, the superiority of BME analysis over STK was amply demonstrated by means of interpolation error maps, correlation scattergrams, space–time accuracy statistics, etc. Significant improvements are possible within the methodological context of MSG. Thus, two computational BME–based techniques were considered in this paper. The BME2, which, by accounting for soft information available at the interpolation points (in addition to the data points) led to improved TO_3 predictions compared to these obtained by BME1 (which considered soft information at the data points only). BME techniques also remove the spatial aliasing problem with the SBUV data, allowing the resolution of zonal wave number smaller than 7. Furthermore, these techniques will create improvements in the latitude–longitude mapping of the stratospheric ozone from the SBUV instrument (although, in this case, it may not improve SBUV profile information).

Several (theoretical and computational) studies are found in the MSG literature, which demonstrate the power and versatility of the BME techniques. BME produces high-resolution analyses with better accuracy than conventional techniques, since it provides improved representations of the composite space–time variability. It does not require the limited modeling assumptions of conventional techniques, and it can incorporate various sorts of uncertain data (e.g., [11] and [33]). Bogaert [4] and D'Or and Bogaert [17] showed that BME is an efficient approach for modeling categorical information that is in many ways superior to the indicator cokriging method. Christakos *et al.* [13] compared BME with Kalman filters (ordinary and extended) and stressed out some advantages of the former over the latter when mapping spatiotemporal processes. Moreover, BME derives a large class of statistical interpolation methods (e.g., Wiener–Kolmogorov filters; simple, ordinary, and intrinsic

kriging) as its special cases under limiting conditions on the modeling assumptions and knowledge bases used—a fact that demonstrates the generalization power of the BME method.

It was noticed that it was not the goal of the TO_3 study presented in this paper to account for PDE atmospheric models, as do certain data assimilation systems (e.g., [16]). Nevertheless, such models can be integrated and processed by BME. Christakos [10], for example, has shown that a variety of physical laws are efficiently accounted for by BME and other MSG techniques. Kolovos *et al.* [24] used BME as an assimilation technique to process the combined model information (advection–reaction PDE) about the dynamics of pollutant processes with hard and soft observations to generate maps of probability distributions across space and time. Also, Christakos [12] presented a methodological comparison between BME and standard techniques of atmospheric data analysis, whereas Serre *et al.* [33] studied PDE models in the context of the inverse problem. As these studies showed, BME analysis has certain interesting advantages compared to standard data assimilation techniques using PDE models, e.g., while many standard assimilation techniques produce unique realizations of the atmospheric fields at a grid of space–time points or derive a set of low-order moments, the BME analysis offers a complete series of pdfs at each point, pairs, or triplets of points, etc. associated with a range of possible solutions.

Ergo, the BME theory can be used to its fullest ability: 1) by focusing on the use of uncertain SBUV datasets to generate analyses of stratospheric ozone (accounting for differences in the level of accuracy between the SBUV and TOMS instruments, developing improved analyses of the TOR, etc.); 2) by integrating other soft knowledge sources, like potential vorticity data and temporal information in the data; and 3) by assimilating into more sophisticated atmospheric models. The items 1)–3) above are important research and development issues that should be the topics of future work.

REFERENCES

[1] C. Appenzeller, A. K. Weiss, and J. Staehelin, "North atlantic oscillation modulates total ozone winter trends," *Geophys. Res. Lett.*, vol. 27, no. 8, pp. 1131–1134, 2000.

[2] P. K. Bhartia, R. D. McPeters, C. L. Mateer, L. E. Flynn, and C. Wellemeyer, "Algorithm for the estimation of vertical ozone profile from the backscattered ultraviolet (BUV) technique," *J. Geophys. Res.*, vol. 101, pp. 18 793–18 806, 1996.

[3] P. K. Bhartia, private communication, 1999.

[4] P. Bogaert, "Spatial prediction of categorical variables: The Bayesian maximum entropy approach," *Stoch. Environ. Res. Risk Assess.*, vol. 16, no. 6, pp. 425–448, 2002.

[5] V. Cherkassky and F. Muller, *Learning From Data*. New York: Wiley, 1998.

[6] G. Christakos, "On certain classes of spatiotemporal random fields with application to space–time data processing," *IEEE Trans Syst., Man, Cybern.*, vol. 21, pp. 861–875, July-Aug. 1991.

[7] ——, *Random Field Models in Earth Sciences*. San Diego, CA: Academic, 1992.

[8] G. Christakos and P. Bogaert, "Spatiotemporal analysis of springwater ion processes derived from measurements at the Dyle Basin in Belgium," *IEEE Trans Geosci. Remote Sensing*, vol. 34, pp. 626–642, May 1996.

[9] G. Christakos and V. Vyas, "A composite spatiotemporal study of ozone distribution over eastern United States," *Atmos. Environ.*, vol. 32, no. 16, pp. 2845–2857, 1998.

[10] G. Christakos, *Modern Spatiotemporal Geostatistics*, 3rd ed. New York: Oxford Univ. Press, 2000.

[11] G. Christakos, M. L. Serre, and J. Kovitz, "BME representation of particulate matter distributions in the state of california on the basis of uncertain measurements," *J. Geophys. Res.*, vol. 106, no. D9, pp. 9717–9731, 2001.

[12] G. Christakos, "On the assimilation of uncertain physical knowledge bases: Bayesian and non-Bayesian techniques," *Adv. Water Resources*, vol. 25, no. 8-12, pp. 1229–1246, 2002.

[13] G. Christakos, P. Bogaert, and M. L. Serre, *Temporal GIS*. New York: Springer-Verlag, 2002.

[14] S. E. Cohn, "Introduction to estimation theory," *J. Meteorol. Soc.*, vol. 75, pp. 257–288, 1997.

[15] B. Cros, D. Nganga, A. Minga, J. Fishman, and V. G. Brackett, "Distribution of tropospheric ozone in Brazzaville, Congo, determined from ozonesonde measurements," *J. Geophys. Res.*, vol. 97, pp. 12 869–12 876, 1992.

[16] R. Daley, *Atmospheric Data Analysis*. Cambridge, U.K: Cambridge Univ. Press, 1991.

[17] D. D'Or and P. Bogaert, "Combining categorical information with the BME approach," in *Proc. 4th Eur. Conf. Geostat for Environmental Application*, Barcelona, Spain, Nov. 27–29, 2002.

[18] J. Fishman, C. E. Watson, J. C. Larsen, and J. A. Logan, "Distribution of tropospheric ozone determined from satellite data," *J. Geophys. Res.*, vol. 95, pp. 3599–3617, 1990.

[19] J. Fishman and A. E. Balok, "Calculation of the daily tropospheric ozone residual using TOMS and empirically improved SBUV measurements: Application to an ozone pollution episode over the eastern United States," *J. Geophys. Res.*, vol. 104, pp. 30 319–30 340, 1999.

[20] J. Fishman, A. E. Wozniak, and J. K. Creilson, "Global distribution of tropospheric ozone from satellite measurements using the empirically corrected tropospheric ozone residual technique: Identification of the regional aspects of air pollution," *Atmos. Chem. Phys.*, vol. 3, pp. 893–907, 2003.

[21] J. F. Gleason and R. D. McPeters, "Corrections to the Nimbus 7 solar backscatter ultraviolet data in the "nonsync" period (February 1987 to June 1990)," *J. Geophys. Res.*, vol. 100, pp. 16 873–16 877, June 1995.

[22] P. Goovaerts, *Geostatistics for Natural Resources Evaluation*. New York: Oxford Univ. Press, 1997.

[23] L. Hood, S. Rossi, and M. Beuten, "Trends in lower stratospheric zonal winds, Rossby wave breaking behavior, and column ozone at northern midlatitudes," *J. Geophys. Res.*, vol. 104, pp. 24 321–24 339, 1999.

[24] A. Kolovos, G. Christakos, M. L. Serre, and C. T. Miller, "Computational BME solution of a stochastic advection-reaction equation in the light of site-specific information," *Water Resources Res.*, vol. 38, no. 12, pp. 1318–1334, 2002.

[25] J. Kovitz and G. Christakos, "Assimilation of fuzzy data by the BME method," *Stoch. Environ. Res. Risk Assess.*, vol. 18, 2004.

[26] P. F. Levelt, M. A. F. Allaart, and H. M. Kelder, "On assimilation of total ozone satellite data," *Ann. Geophys.*, vol. 14, pp. 1111–1118, 1996.

[27] D. S. Lemons, *Perfect Form: Variational Principles, Methods and Applications in Elementary Physics*. Princeton, NJ: Princeton Univ. Press, 1997.

[28] J. Peixoto and A. Oort, "The physics of climate," *Rev. Mod. Phys.*, vol. 56, pp. 365–429, 1984.

[29] W. J. Randel and J. B. Cobb, "Coherent variations of monthly mean total ozone and lower stratospheric temperature," *J. Geophys. Res.*, vol. 99, pp. 5433–5447, 1994.

[30] J. Richardson, "An Investigation of large-scale tropical biomass burning and the impact of its emissions on atmospheric composition," P.h.D. dissertation, Georgia Inst. Technol., Atlanta, 1994.

[31] S. D. Schubert and M.-J. Munteanu, "An analysis of tropopause pressure and total ozone correlations," *Mon. Weather Rev.*, vol. 116, pp. 569–582, 1988.

[32] M. L. Serre and G. Christakos, "Modern geostatistics: Computational BME in the light of uncertain physical knowledge—The Equus Beds study," *Stoch. Environ. Res. Risk Assess*, vol. 13, no. 1, pp. 1–26, 1999.

[33] M. L. Serre, G. Christakos, H. Li, and C. T. Miller, "A BME solution of the inverse problem," *Stoch. Environ. Res. Risk Assess*, vol. 17, pp. 354–369, 2003.

[34] M. L. Stein, *Interpolation of Spatial Data*. New York: Springer-Verlag, 1999.

[35] W. Steinbrecht, H. Claude, U. Kohler, and K. P. Hoinka, "Correlation between tropopause height and total ozone: Implications for long-term trends," *J. Geophs. Res.*, vol. 103, pp. 19 183–19 192, 1998.

[36] F. M. Vukovich, V. G. Brackett, J. Fishman, and J. E. Sickles, II, "On the feasibility of using the tropospheric ozone residual for nonclimatological studies on a quasi-global scale," *J. Geophys. Res.*, vol. 101, pp. 9093–9105, 1996.

[37] ——, "A 5-year evaluation of the representativeness of the tropospheric ozone residual at nonclimatological periods," *J. Geophys. Res.*, vol. 102, pp. 15 927–15 932, 1997.
[38] J. M. Wallace and P. V. Hobbs, *Atmospheric Sciences—An Introductory Survey*. San Diego, CA: Academic, 1977.
[39] J. R. Ziemke and S. Chandra, "Comment on "Tropospheric ozone derived from TOMS/SBUV measurements for TRACE A" by Fishman *et al.*," *J. Geophys. Res.*, vol. 103, pp. 13 903–13 906, 1998.

George Christakos received the M.Sc. degree in soil mechanics from the University of Birmingham, Birmingham, U.K., in 1980, the M.S. degree in civil engineering from the Massachusetts Institute of Technology, Cambridge, in 1982, the Ph.D. degree in mining and metallurgical engineering from the National Technical University of Athens, Athens, Greece, in 1986, and the Ph.D. degree in applied sciences from Harvard University, Cambridge, MA, in 1990

He is currently a Professor and Director of the Center for the Integrated Study of the Environment (CISE), University of North Carolina, Chapel Hill. His group is responsible for significant developments in the fields of science-based spatiotemporal mapping, atmospheric data analysis, flow and transport phenomena, pollution monitoring and control, human exposure analysis, health risk assessment, modern spatiotemporal geostatistics, and advanced functions of temporal GIS. He is the author of three books: *Random Field Models in Earth Sciences* (San Diego, CA: Academic), *Spatiotemporal Environmental Health Modeling* (Amsterdam, The Netherlands: Kluwer), and *Modern Spatiotemporal Geostatistics* (Oxford, U.K.: Oxford University Press). He is the editor of the journal *Stochastic Environmental Research and Risk Assessment*.

Alexander Kolovos received the Ph.D. degree in environmental sciences and engineering from the University of North Carolina (UNC), Chapel Hill, in 2001.

From 1991 to 1995, he was a Research Fellow with the Foundation of Research and Technology Hellas performing computational investigations on water resources and the associated climatic change impact. Most recently, he has been a Postdoctoral Research Associate with the Center for the Integrated Study of the Environment (CISE), UNC. His primary interests are in the area of stochastic computational research. He specializes in numerical modeling of natural systems and multidisciplinary integration in uncertain environments. Some of the fields he has applied his research include atmospheric pollution monitoring and control, environmental health and human risk assessment, whereas his work also led him to investigations on advanced stochastic PDE techniques.

Marc L. Serre received the M.S. degree in civil and environmental engineering from the University of Iowa, Iowa City, in 1992, and the Ph.D. degree in environmental sciences and engineering from the University of North Carolina (UNC), Chapel Hill, in 1999.

From 1992 to 1995, he was Senior Product Manager for hydrology and hydraulic computer-aided design software at Eagle Point, Inc. From 1999 to 2000, he was a consulting expert in air pollution exposure mapping at the US-AID-funded Cairo Air Improvement Program in Cairo, Egypt. Since 2000, he has joined the Department of Environmental Sciences and Engineering, UNC, where he is currently an Assistant Professor. His main research interests are in spatiotemporal modeling and health risk assessment, in temporal GIS, and in the numerical development of advanced mapping functions. He has coauthored a book on advanced functions for temporal GIS, and he manages and develops the BMELIB software for advanced geostastistical functions and space–time data assimilation that is used over 20 countries worldwide.

Fred Vukovich received the M.S. and Ph.D. degrees in meteorology from St. Louis University, St. Louis, MO, in 1963 and 1966, respectively.

He is currently a Chief Scientist with Science Applications International Corporation, Raleigh, NC. He has broad experience in research on climatology, meteorology, oceanography, atmospheric chemistry, and land surface processes using satellite remote sensing data. He has applied satellite remote sensing data in environmental research since 1960, using infrared, visible, and microwave remote sensing data from instruments on satellites such as Explorer VII, TIROS, TIROS-N, NIMBUS, NOAA, HCMM, LANDSAT, GOES, DMSP, TOPEX, SEASAT, ERS-1, ERS–2, and SeaWiFS. He was a member of the SEASAT "Proof of Concept" Team for microwave and infrared remote sensing of the oceans from 1976 to 1979. From 1994 to 2004, he has applied satellite data in studies involving land processes associated with the drought in the Sahel of Africa, deforestation in Rodonia, Brazil, Red Tide off the North Carolina coast, shelf circulation in the Gulf of Mexico, and TOMS/SBUV tropospheric ozone. His most recent efforts have focused on the development of a parameterization scheme based on ground cover characterizations using remote sensing data for improving surface heat flux estimates in global climate models and on the application of analyses derived from satellite remote sensing data to evaluate ocean circulation modeling results. He has been involved in research associated with TOMS data and with the determination of the tropospheric ozone residual (TOR) since the mid-1980s, and he has helped to develop the technique presently being used to estimate the TOMS/SBUV TOR. He led the effort in the evaluation of the TOMS/SBUV TOR data that has been processed at nonclimatological time scales.